Taylor & Francis
Taylor & Francis Group

Check for updates

Biotic and Abiotic Imprints on Mg-Rich Stromatolites: Lessons from Lake Salda, SW Turkey

Nurgul Balci[a], Yagmur Gunes[a], Jérôme Kaiser[b], Sena Akcer On[c], Kadir Eris[a], Bradley Garczynski[d], and Briony H. N. Horgan[d]

[a]Faculty of Mines, Department of Geological Engineering, Istanbul Technical University–Ayazaga Campus, Istanbul, Turkey; [b]Leibniz-Institute for Baltic Sea Research (IOW), Rostock, Germany; [c]Faculty of Engineering, Department of Geological Engineering, Muğla Sıtkı Kocman University, Muğla, Turkey; [d]Department of Earth, Atmospheric, and Planetary Sciences, Purdue University, West Lafayette, IN, USA

ABSTRACT

Modern hydrated Mg rich stromatolites are actively growing along the shallow shorelines of Lake Salda (SW Turkey). An integrated approach involving isotopic, mineralogical, microscopic, and organic/geochemical techniques along with culture-independent molecular methods were applied to various lake samples to assess the role of microbial processes on stromatolite formation. This study further explores the biosignature preservation potential of fossil stromatolites by comparing with textures, lipid profiles and isotopic composition of the modern stromatolites. Similar lipid profile and $\delta^{13}C$ isotope values in active and fossil stromatolites argue that CO_2 cycling delicately balanced between photosynthetic and heterotrophic (aerobic) activity as in the active ones may have regulated stromatolite formation in the lake. A decrease in the exopolymeric substances (EPS) profile of the mat and concurrent hydromagnesite precipitation imply a critical role for EPS in the formation of stromatolite. Consistently, a discrete, discontinuous lamination and clotted micropeloidal textures with cyanobacterial remnants in the fossil stromatolites likely refer to partial degradation of EPS, creating local nucleation sites and allowing precipitation of hydrated Mg minerals and provide a link to the active microbial mat in the modern stromatolites. Our results for the first time provide strong evidence for close coupling of cyanobacterial photosynthesis and aerobic heterotrophic respiration on hydromagnesite textures involved in the stromatolite formation of Lake Salda. The creation of photosynthesis induced high-pH conditions combined with a change in the amount and properties of the EPS and the repetition of these processes over time seems to be a possible pathway for stromatolite growth in the lake. Understanding these microbial symbioses and their mineralized records may provide new insights on the formation mechanism of Mg-rich carbonates not only for terrestrial geological records but also for planetary bodies like Mars, where hydrated Mg-carbonate deposits have been identified in possible paleolake deposits at Jezero crater, the landing site of the NASA Mars 2020 rover.

Introduction

Microbial carbonates formed as a result of atmosphere–biosphere interactions exist from Archean to present day (Awramik and Grey 2005; Chagas et al. 2016; Frantz et al. 2015; Grotzinger and Knoll 1999; Hofmann et al. 1999; Schopf 2006). One of the best examples of such structures are stromatolites, which are defined as organosedimantary structures, representing the oldest fossils on Earth (Allwood et al. 2006; Grotzinger and Knoll 1999). These unusual carbonates first appeared in the Archean 3.5 billion years ago and flourished in the Proterozoic time (about 2500–500 million years ago) (Schopf 2006). The reason why a nosedive in their morphological and textural diversity occurred in the Phanerozoic era is still unsolved. Despite extensive research comprising, sedimentological, geochemical and micropaleontologic features of ancient stromatolites, the controversy

about the origin of these carbonate-bearing rocks still exists (Awramik and Grey 2005; Grotzinger and Knoll 1999). Various experimental studies on a purely chemical basis and mathematical models proposed an abiotic model for stromatolite development and further emphasize difficulties in interpreting the origin of ancient stromatolites (Allwood et al. 2006; Batchelor et al. 2005; Corsetti and Storrie-Lombardi 2003; Grotzinger and Rothman 1996; Jogi and Runegar 2005). Based on comparison with modern stromatolites, various microbial processes such as cyanobacterial oxygenic photosynthesis (Altermann et al. 2006; Riding 2006), anoxygenic photosynthesis (Bosak et al. 2007) and sulfur metabolism (Wacey et al. 2011) have been suggested for the formation of ancient stromatolites. Additionally, the interpretation of structures observed in thick Archean sedimentary sequences as microbially deposited stromatolites

---

along with putative cyanobacterial microfossils reported in the Warrawoona stromatolitic formation further implies that microbial communities, particularly Cyanobacteria, may have contributed to the formation of stromatolites (Allwood et al. 2006; Knoll 2003; Schopf and Packer 1987; Schopf et al. 2007). Despite this extensive research and particularly the lack of microfossils in Precambrian rocks, there is still an on-going debate on how to recognize biotic and abiotic processes involved in the development of stromatolites (Frantz et al. 2015). This long-standing question holds very significant implications in terms of recognizing biological fingerprints in the rock records. Therefore, modern stromatolites provide an excellent natural laboratory to understand and elucidate biotic and abiotic processes controlling the formation of stromatolites and in turn to interpret the ancient analogous.

Today, modern stromatolites form in distinct environmental settings such as open marine, hot springs and hypersaline/alkaline lakes (Chagas et al. 2016 and references therein). Bahamas and Shark Bay stromatolites are well-studied examples of marine stromatolites (Goh et al. 2009; Reid et al. 2000; Visscher et al. 1998) and are considered as good analogs to ancient stromatolites due to their macrofabrics (Reid et al. 2003). Recent studies also revealed that some Archean stromatolites are in fact formed in lakes such as those from the Tumbiana formation (2.7 Ga) (Awramik and Buchheim 2009; Schopf 2006). In contrast to marine stromatolites, lacustrine stromatolites form in a wide range of water chemistries (e.g., fresh, saline) and thus record diverse geochemical conditions in their mineralogy and structure. These features of lacustrine stromatolites along with the discovery of ancient stromatolites with lacustrine origin make them important for exobiology studies (Souza et al. 2012). Therefore, the recent microbial mat development, the key metabolic functions and formation mechanisms of various modern lacustrine microbialites are widely investigated (Gérard et al. 2013, 2018; Kazmierczak et al. 2011; Power et al. 2007; Saghai et al. 2015). Additionally, a couple of studies suggest that water chemistry may in fact influence morphology, microstructure and geochemistry of the microbialites (Awramik and Buchheim 2015; Frantz et al. 2015). Despite these valuable contributions, our knowledge of how physiochemical/geochemical characteristics of water and bio-geochemical parameters can affect and/or regulate formation of stromatolites in different lacustrine environments and most importantly, to what extent biotic and/or abiotic processes can be deduced from the living stromatolites, located in geologically different settings, is still missing.

Hydrated Mg-rich stromatolites in Lake Salda were first documented by Braithwaite and Zedef (1996) and their formation has been solely attributed to cyanobacterial and algal activity (Kaiser et al. 2016; Kazanci et al. 2004; Mavromatis et al. 2015; Russell et al. 1999; Shirokova et al. 2011, 2013). Further studies on the lake have been limited to geochemical and limnological characterization of the lake (Kazanci et al. 2004). Despite the considerable progress, our knowledge about microbial diversity of modern Lake Salda stromatolites, their functional roles in the lacustrine system, and the mineralized records in the fossil stromatolites outcropped around the lake is still limited. Recent mineralogical and geochemical discoveries on Mars have revealed the existence of hydrated Mg-bearing carbonates in Jezero crater, and the fact that NASA has chosen this location as the landing site for its upcoming Mars 2020 rover mission has fueled interests into such environments (Goudge et al. 2015; Salvatore et al. 2018). The Mg-carbonate deposits detected at Jezero may be a result of diagenetically altered hydromagnesite precipitated along the paleolake shoreline (Horgan et al. 2019). Elucidating physicochemical processes responsible for hydromagnesite formation in modern terrestrial environments may provide valuable information for understanding the habitability of early Mars. There are only a few modern lakes on Earth that actively precipitate hydromagnesite and all of these are located within mafic or ultramafic rocks similar to those observed in the Jezero watershed (Garczynski et al. 2019). Of these lakes, Lake Salda is the only deep lake environment and the only one that contains fluvial deltaic input, making the lake an excellent analog for deltaic deposition and carbonate precipitation in a Jezero paleolake.

In this context, our objective is to assess biotic and abiotic fingerprints preserved in Lake Salda's modern and fossil stromatolites to understand processes controlling the formation of stromatolites and to interpret fossil ones preserved in the geological records. For this purpose, an integrated approach combining molecular microbiology, mineralogical, organic and inorganic geochemistry, and petrography was used. Our results may help to delineate major microbial processes responsible for the formation of Mg-rich stromatolites and provide new perspectives on the recognition of the biosignature potential of such environments preserved in the geological records.

Geological setting and lake features

Lake Salda, located in the SW lake district of Turkey at an altitude of 1140 m above sea level, has a surface area of ca. 45 km^2 with an average depth of 80 m and a maximum depth of 200 m. The alkaline (0.015–0.041 mol/L) and magnesium-rich (51–408.4 mg/l) lake is in a closed drainage basin and is perennial. The lake has no visible surface water tributaries except ephemeral small streams and thus the water level is mainly controlled by precipitation and evaporation. A few groundwater seeping is present on the SW and NE part of the lake (Figure 1). An annual-water level fluctuation of ca. 50 cm due to complex interplay of extensive evaporation, irrigational use of the groundwater and karstic aquifers around the lake has been reported by Kazanci et al. (2004). Ultramafic rocks, mainly harzburgite metamorphosed to lizardite in places, are the dominant rocks underlying the main part of lake basin and watershed. Dunite outcrops are locally observed around the lake. Dolomitized Cretaceous limestone underlies the eastern portion of the lake and watershed. The meteoric waters cycling through the ultramafic rocks and ultramafic-derived alluvial fan

Figure 1. Lake Salda sampling sites. Two modern stromatolite sampling sites indicated on the map as S1 and S2 and fossil stromatolites sites (FS1 and FS2) and sub/fossil site (SF1). Lake water (SLW) and groundwaters (SGW) are indicated as a star, and lake sediment (SS) as a circle.

deltas around the SE, SW and NW of the lake cause Mg enrichment and high alkalinity in the lake water (Kazanci et al. 2004).

The modern stromatolites with varying size and surface morphology currently form on both coarse, fine size pebbles and muds in the littoral zone of the lake, particularly along the western (site S1,) and eastern coasts (site S2) (Figure 1, Figure S1). These pebbles (Figure S1(a–d)) and muds (Figure S1(d–f)) are covered by a thick easily dispersed green olive, yellowish pale orange gelatinous materials. Braithwaite and Zedef (1996) reported occurrences of cauliflower stromatolite mounts on the northern part of the lake as well but we do not observe these mounts, most likely eroded by wind and waves. Stromatolite mounts, showing mini columnar structures, with a few centimeters to meters in diameter in shallow and deeper water (ca. 1 m) are present on the eastern shorelines of the lake (site S2) (Figure 1, Figure S1(g,h)). A few small stromatolite islands with cauliflower-shaped stromatolite domes, ca. 10 and 20 m in diameter, are located in SW part of the lake named as Kocalar Burnu (Figure S1(i), Figure 1). These stromatolites rise ca. 8 m above the lake floor and reach ca 2 m of above the lake surface. On the shoreline of Kocaadalar Burnu, stromatolites with a diameter of 20–30 cm also grow on muddy embayments (Figure S1(e,f)). However, extensive human activity caused such unique structures to vanish in these places (Balci et al. 2018).

Materials and methods

Field sampling and analysis

Sampling was conducted on 20 August 2015, and 15 July 2016 and 2017, in different littoral zones of the lake, where

the living and fossil stromatolites are present (Figure 1, Figures S1 and S2). A number of different microbial mat samples ($n = 4$) were collected from the two living stromatolite sites (S1 and S2) (Figure S1, Figure 1). The first site (S1) has a dome and cauliflower-shaped stromatolites (Figure S1(a,b)) and the second site (S2) has a dome and almost tabular shape stromatolites (Figure S1(e,f)). A thick biofilm was often observed on the muddy surface around the lake (Figure S1(d)). At site S1, the stromatolitic mat samples SLM1 and SLM2 were collected from the upper layer of the stromatolites (Figure S1(a–c), Figure 1(a,b)), while SLM3 and SLM4 mats were collected from water depths of 50 cm and 100 cm from stromatolites at site S2, respectively (Figure S1(g,h), Figure 1(e)). A thick biofilm sample was collected from a lizardite pebble at a water depth of ca. 50 cm (OM-1) (Figure 1(f)). All these mat samples were subjected to microbial diversity, optical and scanning electron microscopy (SEM) observations and organic and geochemical analysis. For microbiological analysis, a small portion of the mat sample was collected from each location using a sterile spatula and forceps, placed into sterile 50 ml falcon centrifuge tubes containing a nucleic acid preservation solution (DNA/RNA Shield TM) and stored in a field type cooler and transferred to the laboratory within 8 h. Using these same aseptic techniques, one sediment (SS1) and one water sample (SLW1) were collected from the close vicinity of the mat sampling site (site S2) for microbiological analysis (Figure 1). For scanning electron microscopy – energy dispersive spectroscopy (SEM-EDS-Philips XL30 ESEM-FEG/EDAX system, Philips, Amsterdam, the Netherlands) analyses the mat samples that were freeze-dried and coated by Au/Pd to obtain morphological information at Advanced Technologies Research Center, Bosphorus University. Additionally, the SLM2 mat sample, representing the
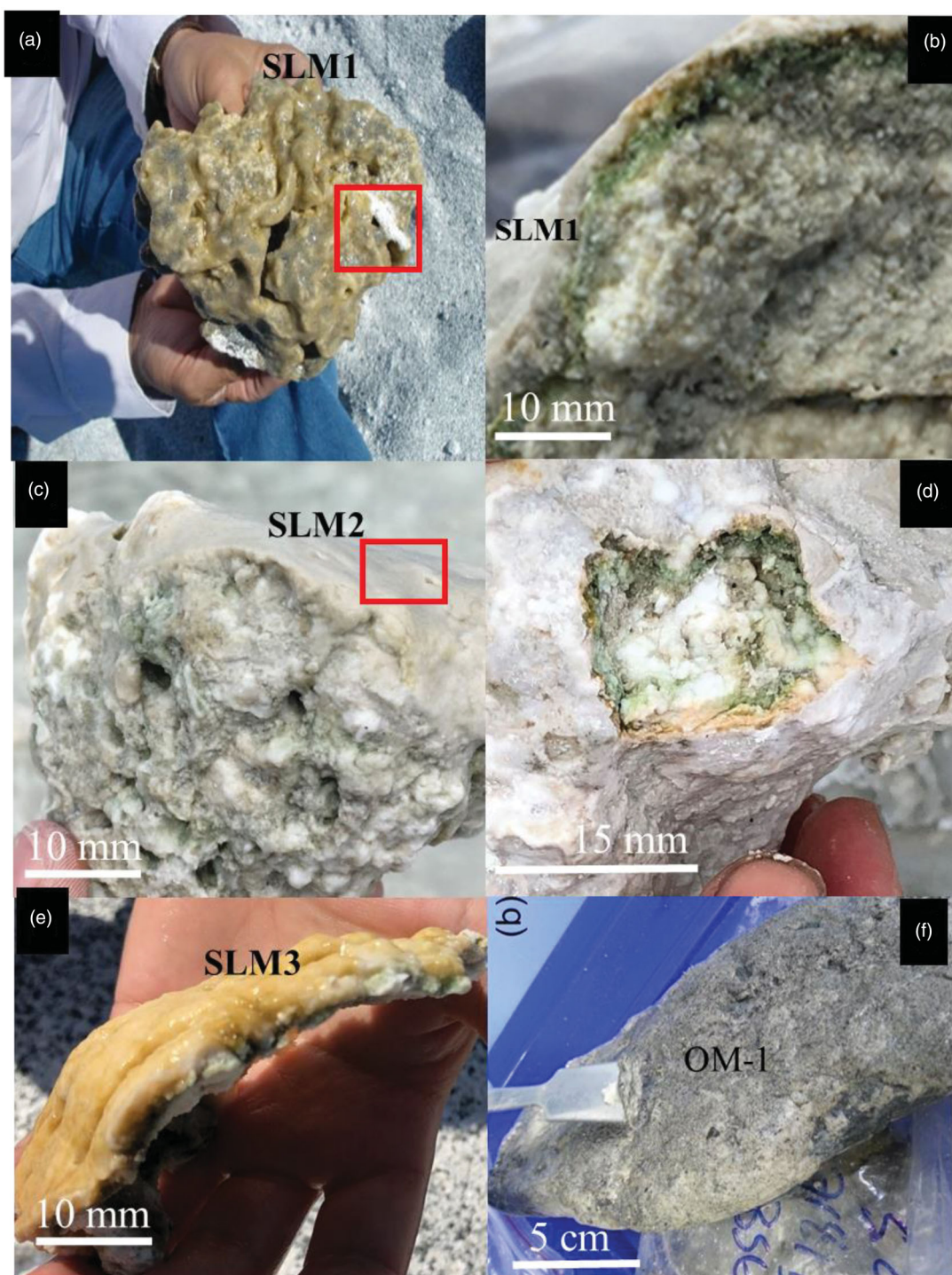
Figure 2. Pictures of mat samples. (a) A smooth green olive mat covering stromatolite domes on Site S1 (Figure S1(a,b)). (b) A closer view of red square in a. Note the color differences. (c) Mat sample from Site S2 (Figure S1(c)). (d) A closer view of red square in (c). Note the similar color development to (b). (e) Microbial mat sample (SLM3) from underwater grown stromatolite with mini columnar structure on Site S2 (Figure S1(g,h)). (f) A large serpentinite grain covered by a thick biofilm (OM-1).

thickest mat (ca. 2.0 cm), was carefully dissected into layers for further detailed microscopic and exopolymeric substances (EPS) analysis (Figure 2(c,d)). The respective mat samples were separated based on the color differences under a dissecting microscope by using a sterile scalpel blade and forceps.

In addition to microbiological analysis, lake surface water (SLW, $n = 9$) and surface sediment (SS, $n = 4$) samples were collected for geochemical analysis (Figure 1). Sediment

samples were collected from the first upper 10 cm of the lakebed surface. Groundwater samples (SGW, $n = 2$) around the lake were collected from wells. For water chemistry analysis, 200 ml water was collected and filtered *in situ* with a single-use syringe filter (Whatmann, 0.2 μm), and 100 ml were saved for anion, cation and alkalinity analyses. The water samples for alkalinity analysis were filled up completely into a Nalgene bottle and tightly closed and prevented from the sunlight. The rest (100 ml) was stored by

adding 1 ml of concentrated ultra-pure HNO_3 acid (Merck) for metal analysis. Major cation analysis (Mg, Ca, Na, K, Si) was carried out by a Perkin Elmer Optima inductively coupled plasma – optical emission spectrometer and anions were analyzed with a Dionex ion chromatography at Istanbul Technical University. Physicochemical properties of water samples (pH, EC, temperature) were measured *in situ* by WTW 333 probe. WTW 333 pH and EC probe were calibrated against to buffer standard solutions at pH 4.01, 7.00, and 9.00 (analytical error: ±0.03 pH units) and at 0.01 mol/L KCl (±0.1 mS/cm), respectively.

The activity of dissolved species and the degree of saturation with respect to main carbonate minerals were determined using the PHREEQC V. 2 hydrogeochemical modeling software (Parkhurst and Appelo 1999). The results of PHREEQC program were presented as saturation index (SI) for each predicted mineral phase where SI = log(IAP/Ksp). IAP is the ion activity product of dissolved mineral constituents in a solubility product (Ksp) for a mineral. SI > 0 indicates oversaturation with respect to the mineral whereas SI < 0 implies undersaturation. The hydrochemical parameters and ion concentration used for all calculations are presented in Table S1.

Mineralogical and geochemical analysis of stromatolites and sediments

For geochemical and mineralogical analyses, fossil (FS, $n = 2$), subfossil (SF2, $n = 1$) and mat (SLM1 and SLM2) samples along with lake surface sediments (SLS, $n = 4$) were used. Fossil stromatolites of FS3 and FS1 were collected from the remnants of stromatolitic domes embedded in hydromagnesite terrace (Figure 1, Figure S2(a–c)), SF2 was collected from sub/fossil stromatolites (Figure S2(i)). A small portion of sub and fossil stromatolites was preserved to make a petrographic thin section for optical microscopy observation and the rest was preserved for radiocarbon dating. Mineralogical composition of the mat, sub/fossil stromatolites and surface sediment samples were determined by X-ray diffractometer(XRD) at Istanbul Technical University (ITU). Each sample (ca. 1 g) was ground in an agate mortar to a powdery size and then thoroughly rinsed with de-ionized water to remove salts and organic particles and allowed to dry at room temperature. The sample was then collected on a silicon sample holder. Measurements were performed with a Bruker diffractometer using CuKα radiation and data were collected between 4 and 90° with a total counting time half an hour. The DIFFRAC.EVA software was used for background subtraction, peak identification and matching with XRD patterns of reference compounds (US Institute of Standards and Technology, UnitedStates). Quantitative analysis was performed using the fundamental-parameter Rietveld refinement programs (BGMN/AutoQuan) (Bergmann et al. 1998; Hillier 2000).

Major and minor elemental chemistry of the samples subject to mineralogical analysis was determined by Inductively Coupled Plasma Mass Spectrometer (ICP-MS; Perkin Elmer). Approximately 0.5 g of each sample split from XRD

analysis was acid digested in a 10 ml volume solution of 5% ultra-pure HNO_3 acid (Merck) and subsequently filtered through a 0.45 μm cellulose acetate single-use syringe filter and used for the ICP-MS analysis

The total organic carbon (TOC) content in the mat, sub/fossil stromatolites and sediments was analyzed with a Shimadzu TOC/TIC analyzer at ITU-EMCOL Geochemistry Laboratory. A complete description of methods used for these analyses can be found in Çağatay et al. (2015). The precision of the TOC analysis with this method is better than 2% at a 95% confidence level.

C And O isotope analysis of stromatolites

The stable carbon isotope composition of all stromatolite samples were obtained from their bulk carbon content (Fossil stromatolites, $n = 6$; living stromatolites, $n = 8$). For living stromatolites, carbonate patches embedded in the mat samples were carefully collected under a dissecting microscope for isotope analysis. Powdered samples were analyzed with a Thermo Delta V Plus mass spectrometer interfaced to an elemental analyzer (EA) at Isotech Laboratories Inc., USA. The carbon and oxygen isotope data are reported in the standard δ-notation relative to the Vienna Peedee Belemnite standard (VPDB). The analytical precision for $\delta^{13}C$ and $\delta^{18}O$ is better than ±0.1‰. Additionally, lake ($n = 3$) and groundwater ($n = 3$) samples were subjected to $\delta^{18}O$ analysis and are reported in the standard δ-notation relative to the Standard Mean Ocean Water (SMOW).

Radiocarbon dating

Radiocarbon dating of sub/fossil stromatolite (FS1, FS3, SF2,) samples were carried out at the Center for Physical Sciences and Technology in Vilnius, Lithuania. For this purpose, bulk stromatolites samples ($n = 3$) were graphitized using a carbonate handling system connected to an automated graphitization equipment AGE-3 (IonPlus AG, Switzerland). The $^{14}C/^{12}C$ ratio of the graphitized rock samples was measured using the 250 kV single stage accelerator mass spectrometer (SSAMS, NEC, USA). The graphitized phthalic acid (Merck KGaA, Germany) was used to estimate the measurement background. It was determined to be 2.45×10^{-3} f_M. The IAEA-C2 standard (pMC value of 41.14 ± 0.03) was used as reference material. For the isotopic fractionation correction, the ratio of $^{13}C/^{12}C$ was used. The obtained radiocarbon ages were calibrated using IntCal13 (Reimer et al. 2013) with a calculated reservoir age of 660 ± 42 years for Lake Salda (Akçer-Ön et al. 2016).

Next generation sequencing (NGS)

The methods used for genomic DNA extraction and Real-time qPCR are provided as supplementary materials (S1) *16S rRNA* V3–V5 regions of genomic DNA isolates were sequenced via NGS. Adapter for Illumina-Miseq and index sequences required each sample to be marked for bacteria and archaea, and integrated to Bact339-F

(5′-CTCCTACGGGAGGCAGCAG-3′)/Bact815-R (5′-CTCC TACGGGAGGCAGCAG-3′) and Arch349-F (5′-GYGCASC AGKCGMGAAW-3′)/Arch806-R (5′-GGACTACVSGGGT ATCTAAT-3″ primer sets, respectively. After DNA libraries were built, filtered, and quality controlled via fluorescent-based measurements, sequencing was performed with an Illumina-Miseq instrument. Sequencing data for an average of 10,000 fragments per library created for each sample was obtained. Reading obtained from sequencing were purified from adapter sequences integrated into each fragment. Using index sequences, samples belonging to each reading were detected and readings were grouped in samples. After cropping adapter and index sequences, readings were subjected to necessary filtering steps with respect to sequence length and quality. Reads containing ambiguous characters and less than 150 nucleotides were removed. The resulting sequences were further denoised by using a pre-clustering method allowing one mismatch (Schloss et al. 2011) and chimeric sequences were removed using chimera uchime (Edgar et al. 2011; Haas et al. 2011). Therefore, high-quality readings were obtained. Each taxonomic level was analyzed using operational taxonomic unit (OTU) classification, BLASTn and GreenGenes databases (DeSantis et al. 2006), and readings per taxonomic levels were detected. OTU classification was performed investigating the clustering of sequences with 97% similarity (Sun et al. 2012). Finally, ratios of microorganisms in each sample were obtained for each taxonomic level and the microbial community was revealed.

Determination of the EPS profile of the mat

The mat sample (SLM2) was used for EPS extraction by closely following the methods published in Decho et al. (2003) and Klock et al. (2007). The mat sample was dissected into four layers (0.5 cm mm^{-1}) and the layers were subsequently mixed with ethylene diaminetetraacetic acid (EDTA, 100 mM) by stirring. The suspension was then centrifuged (15,000 g; 5 min) to separate EPS from cells and detritus. The resulting unfiltered samples were subsequently used to determine the number of EPS. Two different assays were used to estimate the quantity and depth profile of EPS within the mat. The phenol-sulfuric acid assay and the Alcian Blue assay were applied using the methods published in DuBois et al. (1956), Passow and Alldredge (1995), and Bober et al. (2005), respectively. The phenol-sulfuric acid method allows determining the amount of reducing sugars constituting EPS upon hydrolysis, whereas Alcian Blue assays for EPS based on the presence of anionic functional groups (Braissant et al. 2007).

Lipid analysis of stromatolites

The method for lipid extraction and separation has been previously described in Kaiser et al. (2016). Briefly, lipids were extracted of ca. 1 g of dried and homogenized material using an accelerated solvent extraction device (Thermo Scientific™ Dionex™ ASE™ 350) and a mixture of DCM:MeOH (9:1, v:v) as a solvent. After evaporation to dryness, the total lipid extracts were split into four fractions by column chromatography using silica gel as solid phase and hexane:DCM (apolar fraction), and DCM:MeOH (polar fraction) as solvents. Internal standards (squalane, 5α-andro-stan-3β-ol, C$_{46}$ GTGT) added after the extraction was used for quantification.

The apolar and derivatized polar fractions were analyzed by both gas chromatography mass spectrometry and gas chromatography flame ionization detection as described in Kaiser et al. (2016). Before derivatization, the polar fractions containing isoprenoid and branched glycerol dialkyl glycerol tetraethers (iGDGTs and bGDGTs, respectively) were analyzed by high-performance liquid chromatography atmospheric pressure chemical ionization mass spectrometry (HPLC APCI-MS) as described in Kaiser et al. (2016) except for a small modification. Following Hopmans et al. (2016), the separation of the individual GDGTs was achieved on two UHPLC silica columns (BEH HILIC, 2.1 mm × 150 mm, 1.7 μm; Waters™) in series, fitted with a pre-column of the same material (Waters™) and maintained at 30 °C. Using a flow rate of 0.2 ml/min, the gradient of the mobile phase was first held isocratic for 25 min with 18% solvent B (n-hexane:isopropanol, 9:1, v:v) and 82% solvent A (n-hexane), followed by a linear gradient to 35% solvent B in 25 min, followed by a linear gradient to 100% solvent B in 30 min. The column was further equilibrated with 18% solvent B for 20 min before the next run. Note that hydroxylated iGDGTs were not analyzed in the present study.

Results

Hydrochemistry

The physicochemical and chemical parameters of the lake and groundwater were measured during three different field campaigns (2015, 2016, 2017) and the average values of these 3 years' measurements for each parameter are presented in Table S1. Due to the visual observations of increasing mat development on gravels in the shorelines of lake and summer temperature ranges favoring photosynthetic activity a special interest has been put on summer sampling campaigns for lake water chemistry. The average surface water temperature was around 27.5 °C and the highest temperature was measured in August as 35.4 °C. pH ranged from 8.6 ± 0.04 to 9.4 ± 0.03 and dissolved oxygen concentration from 5.1 to 8.3 mg/l with lowest values in the small lagoon water separated from the actual lake water on the southern shoreline of the lake (in the vicinity of SLW2) were measured (Figure 1). In contrast to groundwater (salinity, 3.4 g/l) the salinity of lake water ranges from 1.0 to 1.60 g/l, the highest salinity values belong to SLW1 (1.7 g/l) and SLW2 (1.6 g/l) samples. The dissolved major constituents of most lake water samples display the following sequence: $Mg > Cl > Na > K > Ca$ and $SO_4 > NO_3 > NH_4^+$ revealing characteristics of alkaline water chemistry. However, SWL1 and SWL2 water samples display different water chemistry characterized by high concentrations of Cl, Ca, Na, NO_3, particularly SO_4 and more resembling

groundwater characteristics (Table S1). Both water samples were collected nearby the settlements and may carry anthropogenic influences (e.g., Cl) as well (Figure 1). Consistent with the lake water chemistry, the Mg content of groundwater is high but groundwater is more enriched in SO_4, Cl, Ca, Si, and NO_3 (Table S1). A significant difference in Mg/Ca ratio of groundwater (SGW1: 3.68 and SGW2: 0.67) versus lake water exits indicating further enrichment of Mg in the lake water as well as different groundwater recharged zone such as the dolomitized Cretaceous limestone underlying the eastern part of the lake. The high Mg content of the lake along with elevated Mg and Ca content of groundwater imply weathering of ultramafic rocks as a main source of Mg and Ca for water. Compared to groundwater, even higher magnesium content of the lake may result from further leaching of Mg by meteoric water from serpentinite, lizardite and gabbro pebbles in alluvial fan deltas covering catchment areas around the lake, particularly the SW parts of the lake nearby Kocaadalar Burnu (Figure 1). The lack of significant carbonate minerals, high Mg and Fe and low Ca contents of the surface lake sediments further indicate weathering of ultramafic rocks as the main reason for high Mg content in the lake water (Table S2).

Lake water alkalinity ranges from 0.024 to 0.040 mol/l. The main form of dissolved inorganic nitrogen in Lake Salda is nitrate ranging from 0 to 95.3 mg/l. As for ammonia, the highest nitrate concentration was measured in the lagoons where a higher microbial activity was observed (Figure S1(d), field observation of biofilm and gas bubbling). Nitrate concentration of the groundwater was strikingly high in all samples (95.3–32 mg/l) indicating the agricultural influence on groundwater in the region. The dissolved organic carbon (DOC) concentration, which ranges between 5.2 and 32.7 mg/l, is significantly higher in the water samples where the active growth of stromatolite and mat samples was observed (Figure S1). SI calculation for the lake and groundwater showed that the lake water, with positive saturation indices, was saturated with respect to the main carbonate minerals dolomite (SI > 3.48), huntite (SI > 2.31), magnesite (SI > 2.48), calcite (SI > 0.56) and aragonite (SI > 1.26). Unlike nesquehonite (SI < −0.75) lake water was also saturated in hydromagnesite (SI > 2.3). On the contrary, the saturation indexes for groundwater were always negative (Figure 3).

Mineral, major, and trace element compositions of stromatolites and sediments

The stromatolites of Lake Salda contain 40–49.1% MgO, 1.91–3.11% CaO, 0.18–5.0% Fe_2O_3, 1.04–2.31% SiO_2, and no other elements exceed 1% (Table S2). The general sequence of major ions content in the stromatolites was Mg > Ca > Na > K > Si > Fe > Al. The living stromatolitic mats (SLM1 and SLM2) contain slightly less (up to ca. 7%) MgO than their fossil counterparts. Mineralogical composition of stromatolites is consistent with the chemical analyses, indicating hydromagnesite with a small amount of aragonite as the main carbonate mineral form. The Rietveld
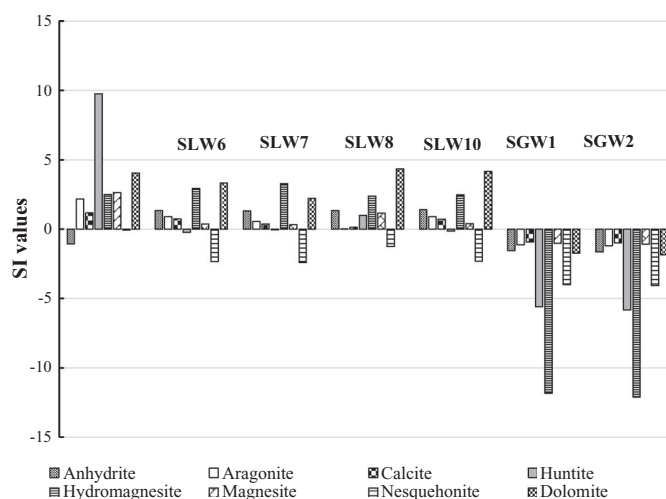
Figure 3. Saturation index values of different minerals calculated for groundwater and lake surface water.
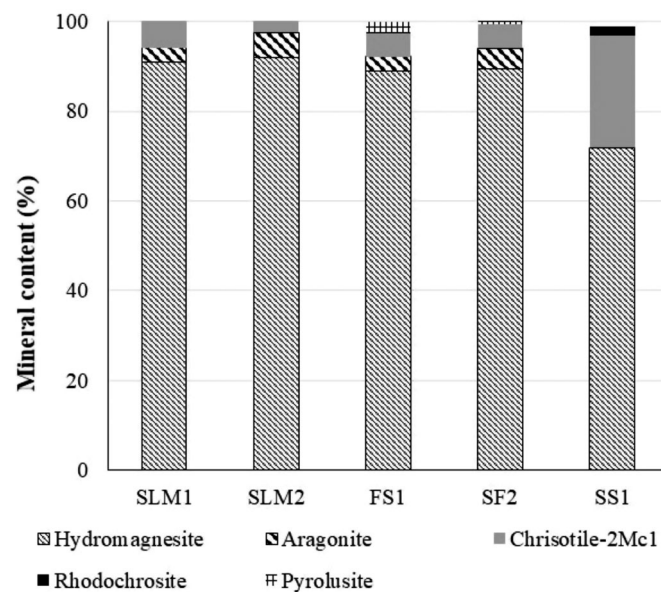
Figure 4. Mineralogical composition of surface sediment (SS1), mat (SLM) fossil (FS) and sub/fossil (SF2) stromatolites (Arg: aragonite; Ctl: chrysotile; Hmg: hydromagnesite; Prs: pyrolusite; Qtz: quartz; Rds: rhodochrosite).

analysis of the active and fossil stromatolites revealed that their hydromagnesite content ranges from ca. 85 to 92% with ca. 3–5% aragonite (Figure 4). Chrysotile was also identified in all samples ranging from 3 to 10%. In the mat samples, hydromagnesite was dominated, particularly where the highest cyanobacteria sequences were identified (SLM1 and 2, Figure 5). Chrysotile was also higher in this mat sample (6.1%) (Figure 4). In contrast, aragonite content of SLM2 mat sample, where the greater number of Firmicutes, α-proteobacteria and γ- proteobacteria were determined, was the highest. Rhodochrosite, pyrolusite and chrysotile are interpreted as likely trapped detrital grains rather than authigenic occurrences (Figure 4). However, occurrences of authigenic Mg silicates in stromatolites have been commonly observed in similar environments (Chagas et al. 2016; Gérard et al. 2018) More interestingly, some Mg silicates associated with manganese are also reported in modern
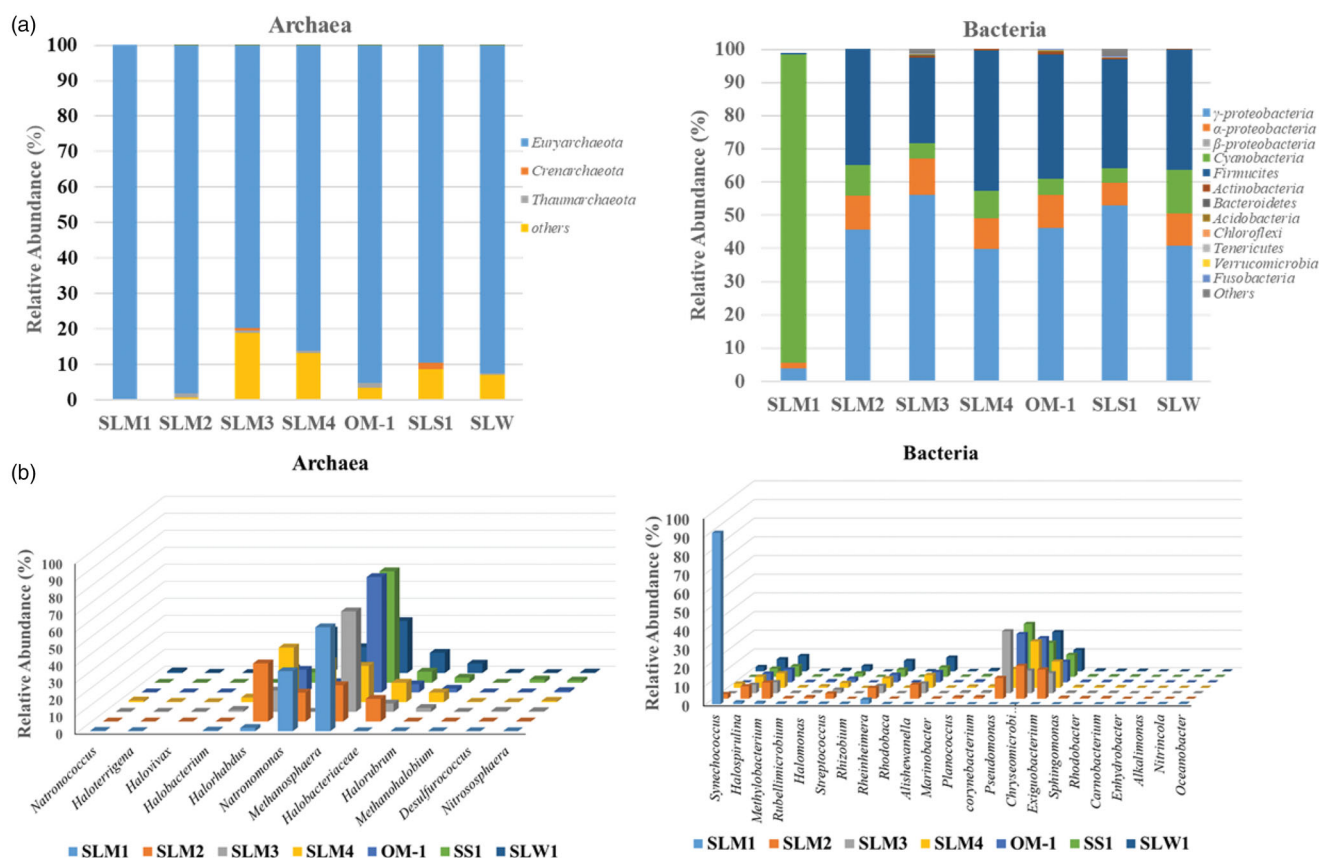
(a)

(b)

Figure 5. Distribution of the relative abundance (%) of bacterial and archaeal *16S rRNA* genes from each sample assigned to different phyla (a) and genera (b).

stromatolites (Zeyen et al. 2015). Presence of high amount of chrysotile particularly in SLM1 mat sample and identified Si peak in SLM1 mat sample along with its high Si content (2.23%) (Figure 6(b), Table S2)) clearly suggest the presence of Mg silicates in the mats although its mineralogy (e.g., chrysotile) is questionable. Therefore, validation of the presence of chrysotile as Mg silicate in the mats deserves more detailed research. Consistently, the sediments collected from the littoral zone of the lake were also dominated by hydromagnesite with chrysotile and a relatively lower amount of aragonite, pyrolusite, and rhodochrosite. Mineralogical composition of the stromatolites are consistent with the lake water chemistry showing high Mg and relatively less Ca content. Si content of the mats (SLM1, SLM2), subfossil (SF2), and fossil (FS1, FS3) stromatolites range from 1.04 to 2.3% (Tables S1 and S2). The mat sample SLM1 with the highest Si content also show high Fe and Mn content. TOC content of the mat samples is significantly higher than the rest of the samples. SLM2 sample even shows a higher value (32.9%) which is consistent with its EPS values (Figure 7). Major and trace elements are more concentrated in stromatolites compared to their ambient waters. Selenium, Ni, Zn, and B content of the mat samples particularly exhibited elevated concentrations (Table S2). The trace element content of stromatolites and sediments are comparable with each other indicating that erosion of the stromatolites is likely a major local source of sediments in the lake.

Radiocarbon age of stromatolites

Fossil FS1, FS3, and SF2 samples yielded corrected age of 750 ± 120, 625 ± 100 years BP and 385 ± 100, respectively, considering a radiocarbon reservoir age of 660 ± 42 years (Akçer-Ön et al. 2016). The reservoir/hard water effect for Lake Salda has been calculated according to analysis on two long (~ 5 m) cores covering the last 4000 years BP (Akçer-Ön et al. 2016). Wood and ostracod shell samples obtained from 64 cm depth on profile dated as ~ 1700 year cal. BP. On the other core Minoan tephra layer and C-14 dated ostracod shells at around 300 cm dated as ~ 3560 years BP. All this point out that ca. 3500–1700 years BP, reservoir age was 660 ± 42 years and did not change through this time interval.

These results are in agreement with the stratigraphic order, that is, FS3 and FS1 were collected from the remnants of stromatolitic domes preserved within the hydromagnesite terrace deposits whereas SF2 was collected from the surface of a subfossil stromatolite (Figure S1(g), Figure S2(c)).

Microbial community composition of Lake Salda stromatolites

The analysis of OTU ($n = 430$ for bacteria and $n = 560$ for archaea) obtained from the mats ($n = 5$), sediment ($n = 1$), and water sample ($n = 1$) revealed that the sequences of bacteria represented around 97% of the total sequences
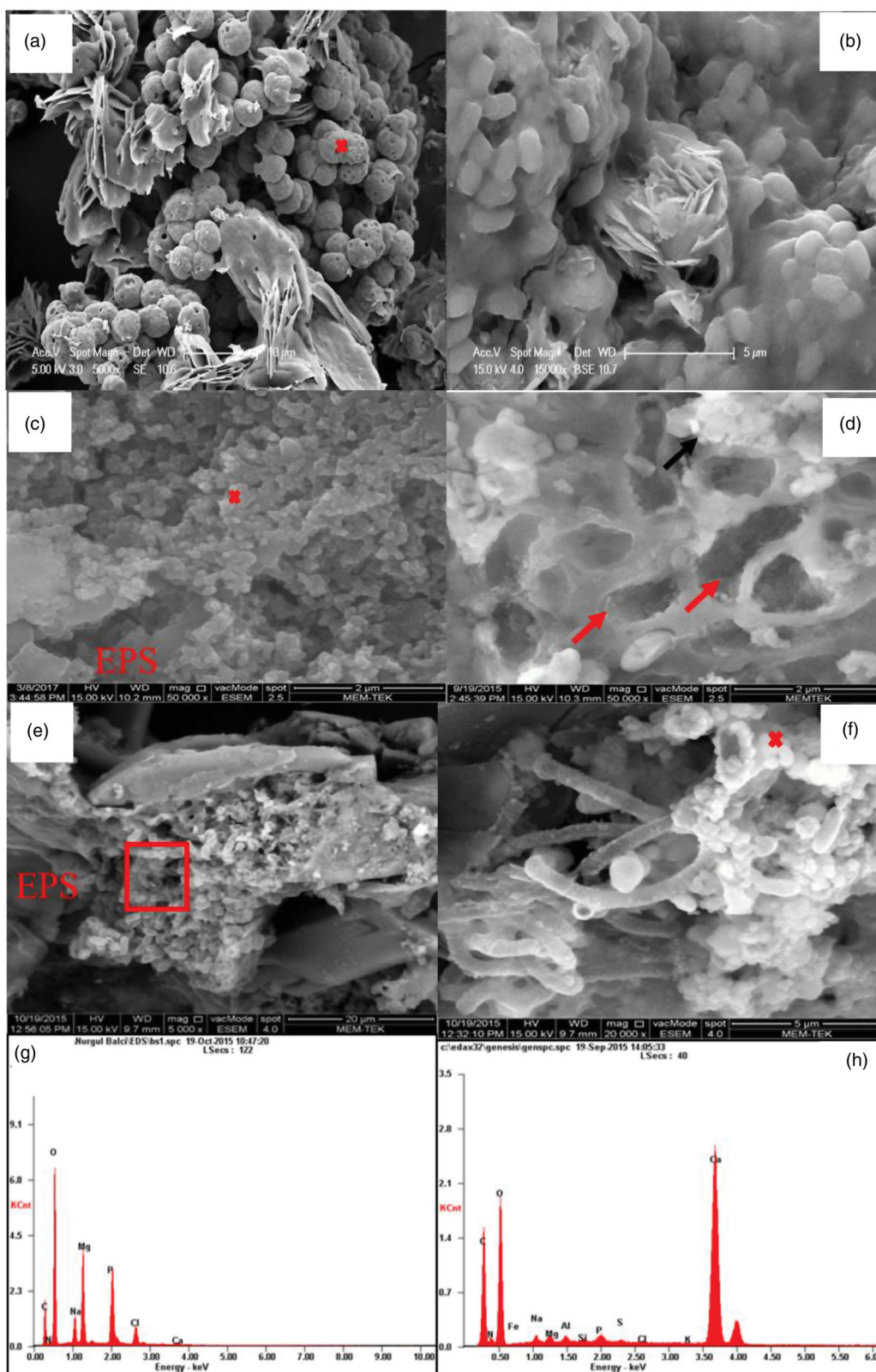
Figure 6. (a) Hydromagnesite spheres showing grape like morphology. (b) Formation of rosette type hydromagnesites among the microbial cells and EPS (arrow). (c) A larger view of symbolled sphere in (a). (d) Bacterial remnant (arrow) with nanosize hydromagnesite (black arrow). (e) Aggregated microbial cells on hydromagnesite flake. (f) A larger view of square in (e), note aragonite nanoglobules around the cells. (g) EDX pattern of the symbol in (c). (h) EDX pattern of the symbol in (f).

compared to those of Archaea (3%) in all samples (Figure 5). A total of 10 phyla of bacteria and three phyla of Archaea were identified in the community (Figure 5(a)). In the bacteria domain, ninety-eight percent of sequences clustered in 5 phyla: Proteobacteria (55.2%) and Firmicutes (30.1%), followed by Cyanobacteria (7.3%), Actinobacteria (1%) and Bacteroidetes (1%), the other phyla were each represented by less than 1% of the sequences and belonged to
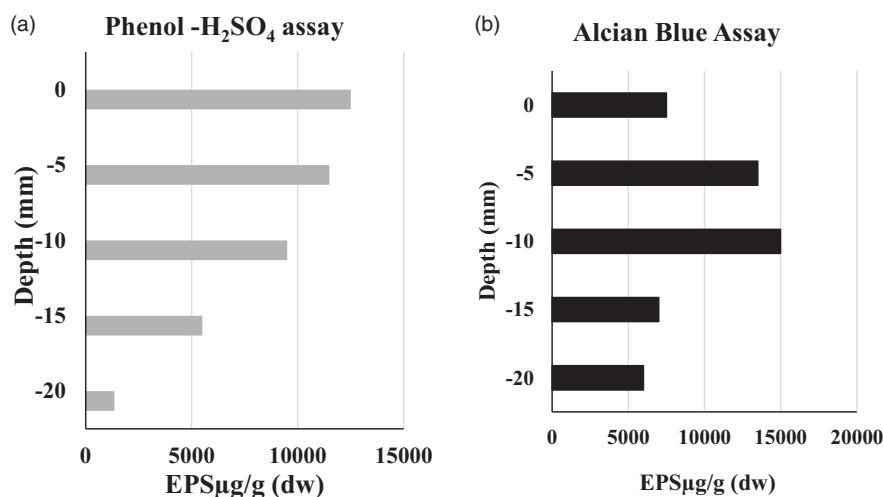
Figure 7. Changes in the amount of EPS with depth in the microbial mat (SLM2). (a) The phenol–sulfuric acid assay. (b) The Alcian Blue assay.

Chloroflexi, Acidobacteria, Verrucomicrobia, Tenericutes, and Fusobacteria.

All Archaea sequences were assigned to the phylum of Euryarchaeota (98%), Thaumarchaeota (1.4%) and Crenarchaeota (<1%). Euryarchaeota phylum was largely dominated in all samples γ-proteobacteria (47.6%) was the most dominant class of the Proteobacteria phylum followed by α-proteobacteria (7.5%), and β-proteobacteria (1%). In the Firmicutes phylum, Bacilli (23.7%) was the dominant class. Actinobacteria was the only class identified in the phylum Actinobacteria. The dominant bacteria genera were represented by sequences of nitrogen-fixing γ-proteobacteria *Pseudomonas* (representing around 25.1% of the total sequences of bacteria), followed by the genera *Chryseomicrobium* (16.8%), *Exiguobacterium* (10.7%), *Methylobacterium* (7.2%), *Alishewanella* (8.4%), *Rheinheimera* (6.6%) and *Rhizobium* (1.4%) (Figure 5(b)).

The distribution of sequences belonging to the different phylum appeared to vary as a function of depth. Cyanobacteria were the third most abundant phylum, in all samples except SLM1 mat sample. Pustular mat samples, SLM1 and SLM2, obtained from the topmost part of cauliflower shape stromatolites comprises the highest percentage of cyanobacteria sequences as 92 and 10%, respectively (Figure 1(a,b), Figure 5(a)). Unicellular *Synechococcus* sp. was the dominant genera in cyanobacteria along with fewer *Halospirulina* genera detected in these mat samples. Morphologically, the cyanobacteria *Lyngba* sp., *Schizothrix* sp., and *Gloeocapsa* sp. were dominated in the uppermost part of the mat sample (SLM1) (Braithwaite and Zedef 1996; Shirokova et al. 2013). Notably, filamentous cyanobacteria stayed dominant only in the superficial mat sample (SLM1), particularly in the green part (Figure 1(b)). SLM2 mat sample was also dominated by Firmicutes (around 42% of the bacteria sequences) and Proteobacteria (up to 40%) mostly presented by γ-proteobacteria (25% of bacterial sequences). Among all the mat samples, Proteobacteria and Firmicutes phylum were largely dominated in SLM3 (up to 67.2 and 25.6%, respectively) and SLM4 (49.1 and 42.4%) mat samples obtained from underwater grown stromatolites with

mini columnar structures. γ-proteobacteria were largely dominated in SLM3 (around 45% of the bacterial sequences) more abundant than Cyanobacteria (only 4%) and Firmicutes (up to 25%). In contrast, Firmicutes dominated the SLM4 sample (up to 42%). Proteobacteria, dominantly presented by γ-proteobacteria (35% of the bacterial sequences) and Firmicutes (up to 39%) were abundantly determined in OM-1 sample recovered from subaqueous lizardite gravel (Figure 1(e,f)) and lake sediment (SS1). Consistent with the sediment sample, Firmicutes phylum were dominated in lake water. As for bacteria, archaeal communities showed differences among the mat samples. The dominant genera of Archaea, *Methanosphaera*, *Halorhabdus*, *Natronomonas*, and *Halobacteriaceae* represented, respectively, 65.1, 9.6, 7.2, and 5.7% of the total sequences of Archaea. Surface mat samples (SLM1 and SLM2) were largely represented by *Natronomonas* (35 and 20%, respectively), *Methanosphaera* (45 and 20%, respectively) and *Halorhabdus* (up to 2 and 40%, respectively). Underwater grown stromatolite mat samples (SLM3 and SLM4) were dominated by *Methanosphaera* (up to 60 and 22%, respectively), *Halobacteriaceae* (5 and 30%, respectively), and *Halorubrum* (up to 3 and 6%, respectively).

Lipid composition of stromatolites

The total contents of the main hydrocarbons, steroids and *n*-alkanols, iGDGTs, and bGDGTs in the samples are heterogeneous and range between 0.5–4.5 µg/g, 2.8–13.6 µg/g, 0.7–47.3 mg/g, and 2–130 mg/g dry weight, respectively. The main hydrocarbon distribution in the samples is dominated by the n-$C_{27:0}$, n-$C_{29:0}$, and n-$C_{31:0}$ alkanes with mean relative concentrations of 6–12% (Figure 7). n-$C_{19:0}$, n-$C_{20:0}$, and n-$C_{21:0}$ alkanes have mean relative concentrations between 4–8%. A $C_{25:2}$ highly branched isoprenoid (HBI) is present with a mean relative concentration of 7%. The relative amounts of the other hydrocarbons present in the samples are <5%. n-C_{18} and n-C_{22} alkanols are the main compounds of the fraction containing steroids and *n*-alkanols (Figure 8). Cholestanol, stigmasterol, dinosterol, and
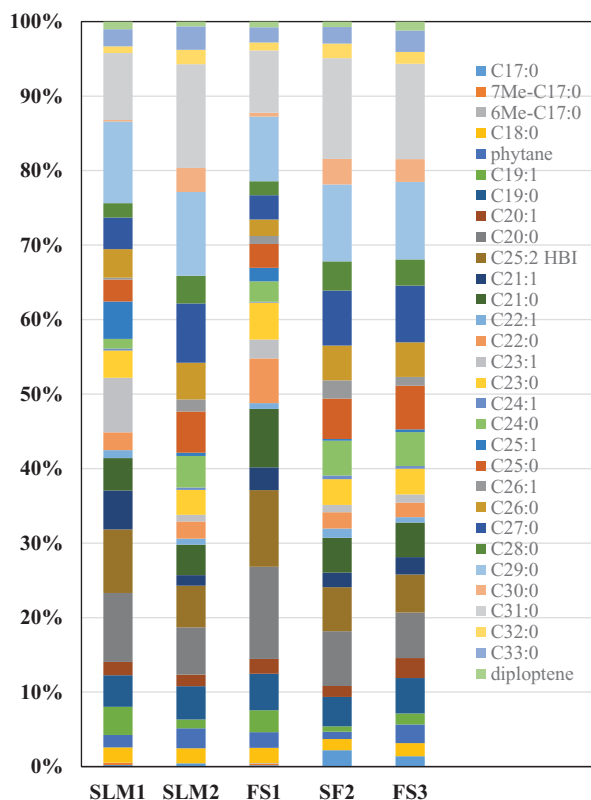
Figure 8. Relative concentrations (%) of the major hydrocarbons detected in living (SLM1 and SLM2) and fossil (FS1, and FS3) and sub/fossil (SF2) stromatolites sampled at locations S1 and S2 in Lake Salda (see Figure S2).

Figure 9. Relative concentrations (%) of the major steroids and n-alkanols detected in living (SLM1 and SLM2) and fossil (FS1 and FS3) and sub/fossil (SF2) stromatolites sampled at locations S1 and S2 in Lake Salda (see Figure S1).

dinostanol have relative concentrations between 6–10%. The analyzed iGDGTs are present in all samples (Figure 9(a)). The distribution of tetramethylated (Ia, Ib, Ic), pentamethylated (IIa, IIa', IIb, IIb', IIc, IIc'), and hexamethylated (IIIa, IIIa', IIIb, IIIb', IIIc, IIIc') bGDGTs is relatively homogenous (Figure 9(b)). bGDGT-Ia, -IIa, -IIb, and -IIIa' have the highest relative concentrations (11–22%). bGDGT-IIc' and -IIIc' were not detected in the samples. The relative concentrations of iGDGT-1, iGDGT-2, iGDGT-3 and cren' remain between 0–10%. The percentage of iGDGT-0 is higher (ca. 85%) in samples SLM1 and FS1, while the percentage of cren is higher (ca. 40%) in samples SLM2, FS2 and FS3 (Figure 10).

Microbial mat structure

Lake Salda microbial mats occur on the surfaces of shallow cauliflower and dome shape stromatolites (Figure S1(a–c)), on muds (Figure S1(d)), pebbles and muddy embayment (Figure S1(e–f)). The surface of submerged stromatolites, particularly those at 1 m depth, are botryoidal and show a few centimeter mini columnar structure covered by orange color dominated gelatinous coatings (Figure S1(g–f)). Microbial mats of cauliflower-shaped stromatolites (SLM1 and SLM2), at the water-air interface, typically have a 1–2 cm thickness representing both poorly- and/or non-lithified characteristics of gelatinous olive green-orange colored pustular smooth mat (Figure S1(a–c)). An endolithic intermixed green and orange colored mat layer is present under this smooth surface
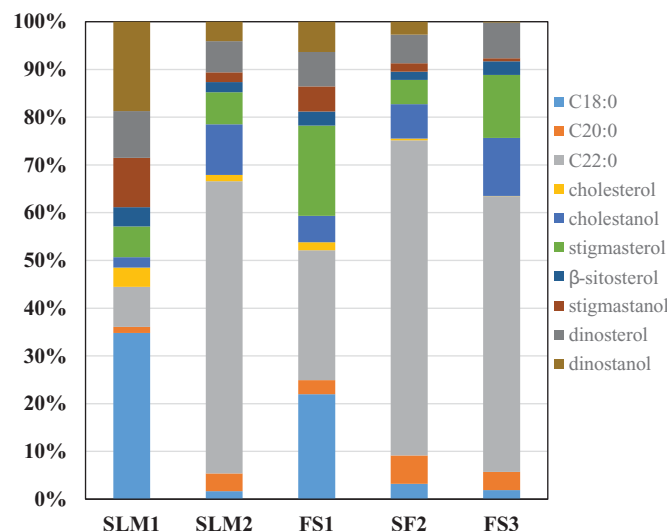
(Figure S1(b,c)). White carbonated patches were often identified beneath the surface layer (Figure 11(a)). Microscopic observation of the dissected parts of the pustular smooth mat (SLM2) revealed various structures (Figure 11). Consistent with molecular analysis, optical observation of the uppermost part of greenish smooth mat surface (SLM2-1; 0–5 mm) revealed filamentous and coccus cyanobacteria consisting of *Schizothrix* sp., and *Synechococcus* sp., and *Gloeocapsa* sp. with a sparse population of *Lyngbya* (Figure 11(a,d)). In general, a cyanobacterial meshwork containing living intertwined filaments concentrated at this uppermost part of the mat. A few diatoms are present within this network (Figure 11(e)). In a deeper horizon of the mat (>10 mm) orange-colored mat is present (SLM2-3, SLM2-4), microbial cells with different shapes (e.g., rod and bacillus) closely associated with the cyanobacterial filaments are identified (Figure 11(e,f)). White and brownish precipitates often occur around the cells (Figure 11(f)). The number of EPS measured throughout the mat profile (SLM2) by the phenol-sulfuric acid assay (PSAA) versus the Alcian Blue assay (ABM) showed some differences (Figure 7). These two assays (PSAA and ABM) provide an estimate of the number of EPS as sugar monomers and the amount of cationic binding sites in the EPS. The most abundant of EPS polymers is associated with the upper 5 mm of the mat and presented by PSAA assay. In this top upper layer (0–5 mm), the number of EPS by PSAA showed a relatively constant distribution following an almost 10-fold decrease (15–20 mm) (Figure 7(a)). A peak at 5–10 mm (1.5×10^4 μg/g EPS) was measured by the ABM assay, a measure of sugar acidity, and EPS decreased by half in the deeper layers (15–20 mm) of the mat which coincided with presence of rod and bacillus shape bacteria (Figures 11(f) and 7(b)).

Macroscopic and textural features of fossil stromatolites

Fossil stromatolites (FS1, FS3) are particularly present along the E (FS1, FS3) and SW part of the lake where thick hydromagnesite terraces are deposited (Figure 1, Figure S2(a,b)).
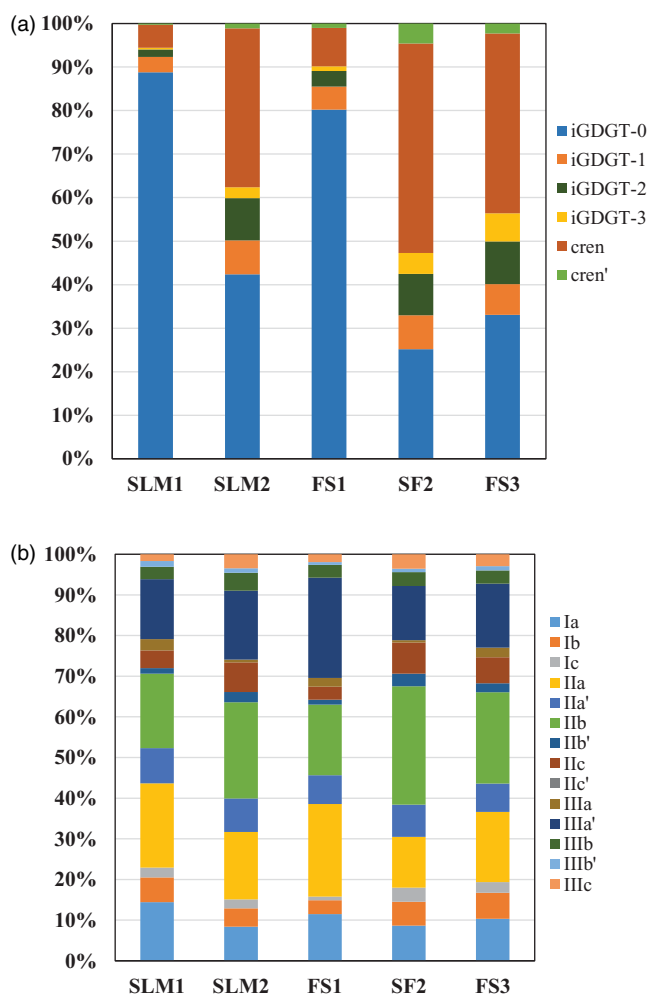
Figure 10. Relative concentrations (%) of iGDGTs (a) and bGDGTs (b) detected in living (SLM1 and SLM2) and fossil (FS1 and FS3) and sub/fossil (SF2) stromatolites sampled at locations S1 and S2 in Lake Salda.

Some of the fossil stromatolites are intercalated with terrace deposits (Figure S2(a)) and remnants of dome structures are preserved in the deposits (Figure S2(b)). The upper part of these terrace deposits shows blocky textures and cavities in the cement (Figure S2(a), small box). Sub/fossil stromatolites occur in the form of cauliflower-like, nearly snow-white, large irregular mounds, domes (Figure S2(c)). These subfossil formations are particularly widespread along the SW part of the lake (Figure 1, Figure S2(c,d)). Their surfaces are partly botryoidal and contain numerous rough knobs and granules in various sizes (Figure S2(c,f,g)). The alternating fine and coarse layers with millimeter-scale are easily observed. A cross-section of sub/fossil stromatolite slab shows mini radial columnar structures with internal layers (Figure S2(d)). Sub/fossil stromatolites with a columnar morphology represent a rectangular (1), convex (2) and parabolic (3) lamination as internal structure (Figure S2(e, f)). Petrographic thin sections prepared from a slab of sub/fossil stromatolite revealed peloidal, microsparitic, and micritic fabrics (Figure 12). On top of the growing direction of the slab, a course lamination with detrital grains on the top was observed (Figure 12(a)). This course lamination with detrital grains likely refer trapping and binding

processes near the surface. The detrital grains 100–500 μm in diameter are composed of small fragments of mafic rocks. A concentrically laminated coliform texture is common on weak lamination composed of micritic and micro sporadic layers (Figure 12(b)). A closer view of the irregular granular laminae reveals peloids and irregularly dispersed spheres (Figure 12(c,d)). The micropeloidal structure and clusters of remnant coccoids are closely associated with peloids in micritic textures(Figure 12(c)). Various size of spheres is common in this layer (Figure 12(d)). In fossil stromatolites, peloidal textures are aggregated by dark micrite surrounded by microspar (Figure 12(e)). In some thin sections, radially fibrous and acicular crystals identified as aragonite in micritic and/or microsparitic fabrics are observed (Figure 12(f)). Examination with petrographic microscopy of fossil stromatolites dated to 750 ± 120 and 650 ± 100 calendar years BP revealed well-preserved remnants of cyanobacterial filaments and diatom frustules in the microfabrics (Figure 12(g,h)). Furthermore, remnants closely resembling rod shape bacteria were occasionally present around the cyanobacterial filaments (Figure 12(h)).

Stable C and O isotopes of stromatolites

The $\delta^{13}C_{carb}$ and $\delta^{18}O_{carb}$ values of stromatolites are presented in Figure 13. The $\delta^{18}O_{carb}$ values of living and sub/fossil stromatolites are positive, ranging from $+5.4$ to $+8.2‰$. These $\delta^{18}O_{carb}$ values correspond to $\delta^{18}O_{V\text{-}smow}$ values ca. $+37$ to $+40‰$ (Coplen et al. 1983). Consistent with $\delta^{18}O_{carb}$values, the $\delta^{13}C_{carb}$ values of all stromatolites are also highly positive ranging from $+2.10$ to $+7.10‰$. The $\delta^{13}C_{carb}$ values of living stromatolites are ca. $+2$ to $+4‰$ depleted in ^{13}C relative to their fossil counterparts, whose $\delta^{13}C$ values fall within a range of $+4.7$ to $+6.9‰$. The $\delta^{18}O_{carb}$ values of living stromatolites clustered in a narrow range with an average value of ca. $+7‰$ being comparable with the fossil ones ($+7.6‰$). No significant correlation exists between $\delta^{18}O_{carb}$ and $\delta^{13}C_{carb}$ values. $\delta^{18}O_{GW}$ values of groundwater have a value of ca. $-8‰$ ($n = 3$), whereas lake water $\delta^{18}O_{LW}$ values approximate $+4‰$ ($n = 4$).

Discussion

Influence of physicochemical parameters on hydromagnesite precipitation

The concentration of magnesium ions is extremely high in a small number of closed lakes, and Lake Salda is one of these. Mg compounds are more soluble than their calcium counterparts and therefore, it is rare for significant amounts of magnesium to precipitate in lakes with normal Mg concentration. Nevertheless, our results demonstrated that hydromagnesite with minor amount (up to 5%) of aragonite precipitates within the mats of the living stromatolites in Lake Salda indicating complex processes regulating precipitation reactions. Mg/Ca ratio of the reactive fluids has been considered as the main factor controlling carbonates mineralogy and formation of hydrated Mg
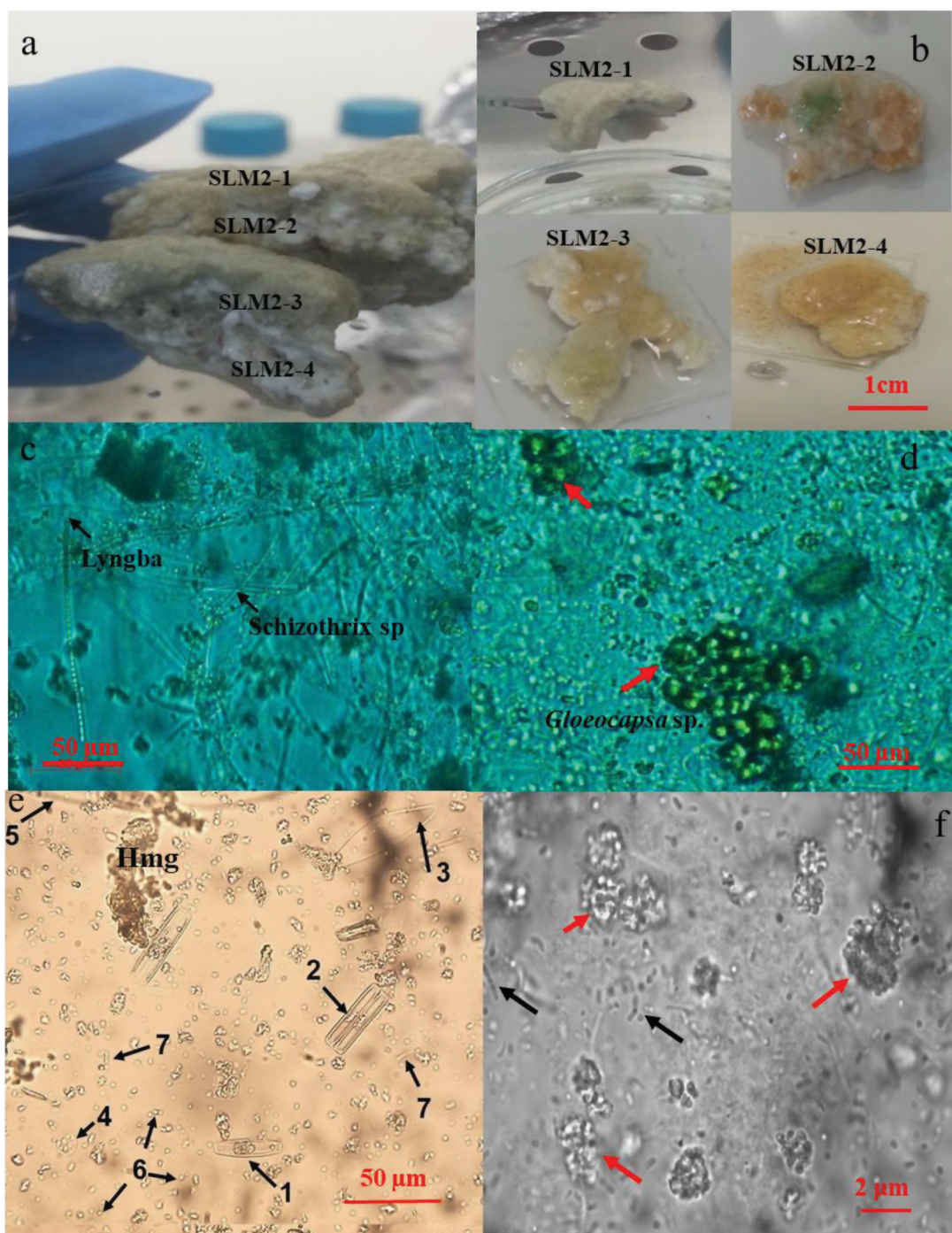
Figure 11. (a) Photomicrographs of the mat sample (SLM 2) and its dissected parts (b). (c, d) A view of intense cyanobacterial filaments of upper 0–5 mm of the mat (SLM2-1) representing meshwork structure. Note the filaments of Schizothrix sp. and Lyngba sp. (d) A view of *Gloeocapsa* sp. in the mat structure (SLM2-2). (e) Mat structure (SLM2-3), (1–4): diatoms; 1: *Navicula* sp.; 2: *Pinnularia* sp., 3: *Amphora* sp.; 4: *Cyclotella* sp. 5: filamentous cyanobacteria; 6: *Cyanobacterial coccus*; 7: rod shaped bacteria. (f) Bacterial cells (rod shapes, black arrow) around carbonate precipitation (the arrow) in the mat sample (SLM2-4). All mat samples were photographed in transmitted plain light except (c) and (d) photographed in fluorescent microscope (10517).

carbonates is usually attributed to high Mg/Ca ratio (>16) under low P_{CO_2} values in lacustrine settings (Hänchen et al. 2008). These unique geochemical environments are usually consistent with alkaline lakes experiencing high evaporation conditions raising an abiotic origin for hydrated Mg carbonates such as hydromagnesite. However, a number of recent studies carried out in different geological settings (e.g., lakes) revealed otherwise and clearly showed microbial influences on precipitation of hydrated Mg carbonate minerals (Gérard et al. 2013, 2018; Kazmierczak et al. 2011; Power et al. 2007; Saghai et al. 2015; Sanz-Montero et al. 2019; Shirokova et al. 2013). Compared to local groundwater, elevated concentration of Mg along with high Mg/Ca ratio measured in the lake water emphasis favorable conditions for chemical precipitation of particularly hydrated Mg carbonates (Table S1, Figure 3). The calculated SI values are in fact consistent with this determination (Figure 3).
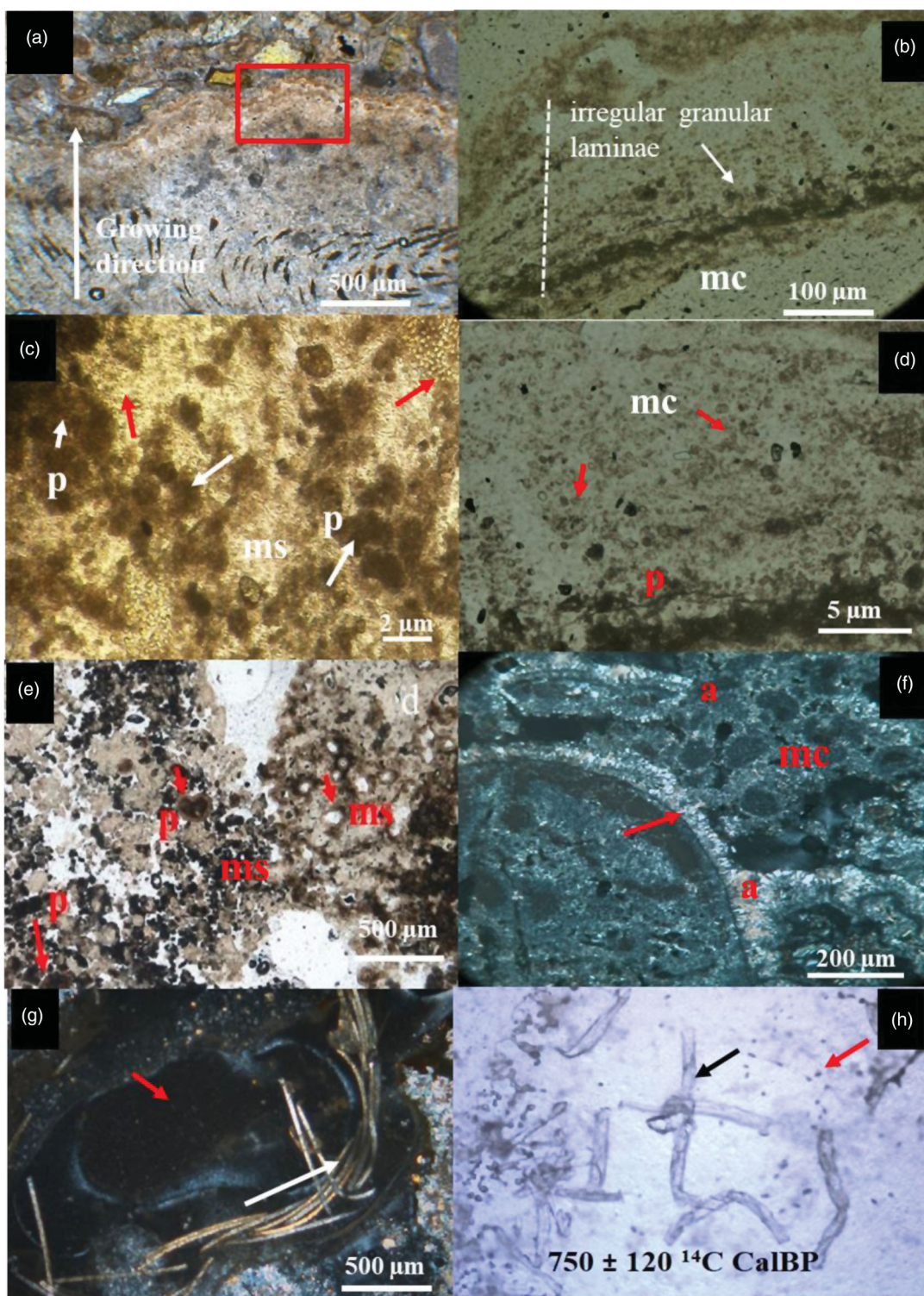
Figure 12. Main textures of sub/fossil and fossil stromatolites. (a) Vertical section of a slab of sub/fossil (SF2) stromatolite (see Figure S2(d)). Laminated and non-laminated textures. Note microstromatolites composed of tiny columns with wavy micritic layers (b–d). A closer view of the square; (b), irregular granular micritic laminae with spherulites and peloids (p). (c) Clotted micropeloids (p, white arrow) and coccus cell remnants (black arrow). (d) Spherulites with different sizes dispersed in micritic and peloidal textures. (e) Peloids (p) and microsparitic textures (ms) of FS3 fossil. (f) Acicular aragonite crystals (a) within the micritic-microsparitic mixed texture of FS1 fossil. (g,h) Relics of microfossil forms in fossil stromatolite of FS3, note calcified filaments in a diatom frustule (g, black arrow) and cyanobacterial filaments (black arrow) and spherical remnants (arrow). All vertical thin-sections were photographed in plain transmitted light.

The SI data obtained from geochemical modeling (PHREEQ-C) of the lake and groundwater suggest that lake water was under-saturated with respect to nesquehonite and anhydrite, nearly saturated with respect to aragonite (average SI: 0.9)) and calcite (SI, 0.6). For hydromagnesite (SI, 2.47) and dolomite (SI, 3.5) the lake water was supersaturated. Similar high SI values to those calculated in this study have been reported in Lake Salda (Shirokova et al. 2013) and other microbialites where a biotic origin were proposed (Kazmierczak et al. 2011; Kempe and Kazmierczak 2007).
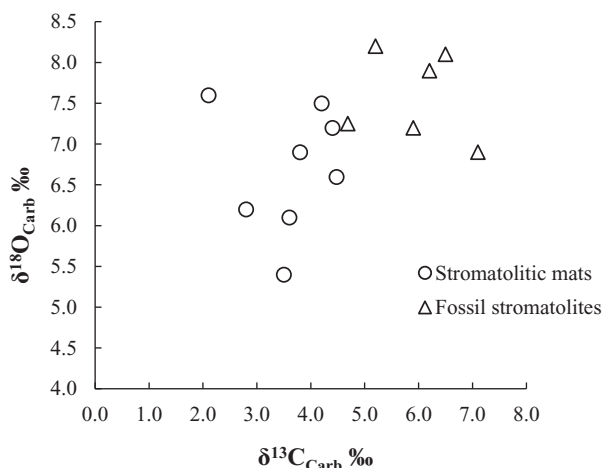
Figure 13. C and O isotope composition of the living and fossil stromatolites. $\delta^{18}O$ value of groundwater ($n = 3$) $\delta^{18}OGW$, $-8‰$ and $\delta^{18}O$ value of lake water ($n = 3$) $\delta^{18}OLW$, $+4‰$).

In contrast to lake water, the groundwaters are strongly under-saturated with respect to hydromagnesite (SI, -11.8) and other main carbonate minerals likely resulting from short percolation times to come equilibrium with these minerals. Under saturation of groundwater with respect to hydromagnesite is not only consistent with the fact that hydromagnesite only precipitates in the lake water but also refer prerequisite of Mg enrichment and thus high Mg/Ca for precipitation in the lake. Although the calculated SI values for lake water indicate favorable chemical conditions not only for hydromagnesite, but also for dolomite and calcite precipitation, the mineralogical compositions of the living and fossil stromatolites as well as lake sediments are in disagreement with the SI values and do not include any carbonate minerals except hydromagnesite and occasionally aragonite (Figure 4). The absence of Mg carbonate precipitation in abiotic and nutrient-free biotic experiments carried with Lake Salda water were reported by Shirokova et al. (2013). Consistent with these results, we observed no direct precipitation from the lake water or evaporated waters on the shoreline of the lake as reported by Braithwaite and Zedef (1996) and Shirokova et al. (2013). Therefore, evaporation alone does not seem to be sufficient to trigger of hydromagnesite precipitation in Lake Salda. Even though the water chemistry of Lake Salda characterized by high pH and Mg/Ca ratio creates supersaturated conditions for Mg carbonates spontaneous precipitation does not occur in the lake. Instead Mg carbonate formation was only observed within the mats implying a critical microbial role in the lake (Braithwaite and Zedef 1996; Mavromatis et al. 2015; Shirokova et al. 2013).

To initiate precipitation of hydrated Mg carbonates, an increase in Mg/Ca ratio along with a decrease in P_{CO_2} should occur. This dual process can occur in the presence of photosynthetic bacteria (e.g., Synechococcus sp.) which uptake of HCO_3^- and release of OH^- ions causing an increase in pH and alkalinity in their microenvironments. The surface of bacterial cells may also act as a nucleation site for Mg and/or Ca ions to initiate kinetically inhibited

precipitation (Benzerara et al. 2006; Dupraz and Visscher 2005). Microbial mats dominated by cyanobacteria at the very top surface of the mat and associated hydromagnesite precipitation suggest that photosynthetically induced pH rise and supersaturation can be an effective way to precipitate hydromagnesite in the lake (Figure 5(a), Figure 11(c), Figure 14(a,b)). Such a role would be consistent with the reports of hydromagnesite forming in association with several different photosynthetic microorganisms (Couradeau et al. 2013; Gérard et al. 2013, 2018; Shiraishi et al. 2008). Lack of free hydromagnesite precipitation in the water column of the lake and presence of hydromagnesite only around the shoreline of the lake where light can easily penetrates emphasis the role of phototrophic activity during hydromagnesite precipitation in the lake.

Microbe–mineral interactions in the mats

Our sequences data revealed that the microbial communities associated with the mats were mainly composed of bacteria (97% of total sequencing), most of which have heterotrophic metabolism whereas archaea constituted only 3% of the total sequencing data. Our results are corroborates with previous studies carried out both at marine (Casaburi et al. 2016) and freshwater microbialites sites (Couradeau et al. 2011; Gérard et al. 2013; Goh et al. 2009; Saghai et al. 2015). Members of the γ-proteobacteria and α-proteobacteria classes of Proteobacteria, Firmicutes, Cyanobacteria and Bacteroidetes were the most abundant bacterial taxa, followed by Verrucomicrobia, Actinobacteria, and Chloroflexi (Figure 5). Although anoxygenic photosynthesizers (e.g., Chloroflexi $<1\%$) and sulfate reducers (Desulfurococcus) were not abundantly determined in the mats, their contributions to carbonate precipitation cannot be excluded in the lake (Visscher et al. 1998; Visscher and Stolz 2005).

Community composition varied among the sites and with water depth of the mat samples. In general, γ-proteobacteria and α-proteobacteria were much less abundant in surface samples where hydromagnesite is only carbonate mineral (SLM1 $< 5\%$ bacterial sequences) as compared to the deeper SLM3 (50 cm) and SLM4 (100 cm) samples, where they accounted for 42 and 10% and 25 up to 10%, respectively . Cyanobacteria were less abundant in the deeper samples (SLM3, SLM4) (up to 9%), but increased their proportions to up to 92% in surface sample (SLM1). Consistently, a high percentage of γ-proteobacteria (up to 55%), α-proteobacteria (up to 30%) with low sequences of Cyanobacteria are reported in microbial community of deeper microbialites in extreme Lake Alchichica, and Lake Van, respectively (Lopez-Garcia et al. 2005; Saghai et al. 2015). In contrast to high abundances of bacteria in the mats and consistent with previous studies low diversity and minor proportion of archaea in the microbial communities of Lake Salda likely refer their minor and/or insignificant roles during stromatolite formation (Allen et al. 2010; Couradeau et al. 2011). Inversely, we observed numerous diatoms in the mat structure suggesting that eukaryotes may in fact play a role during formation of
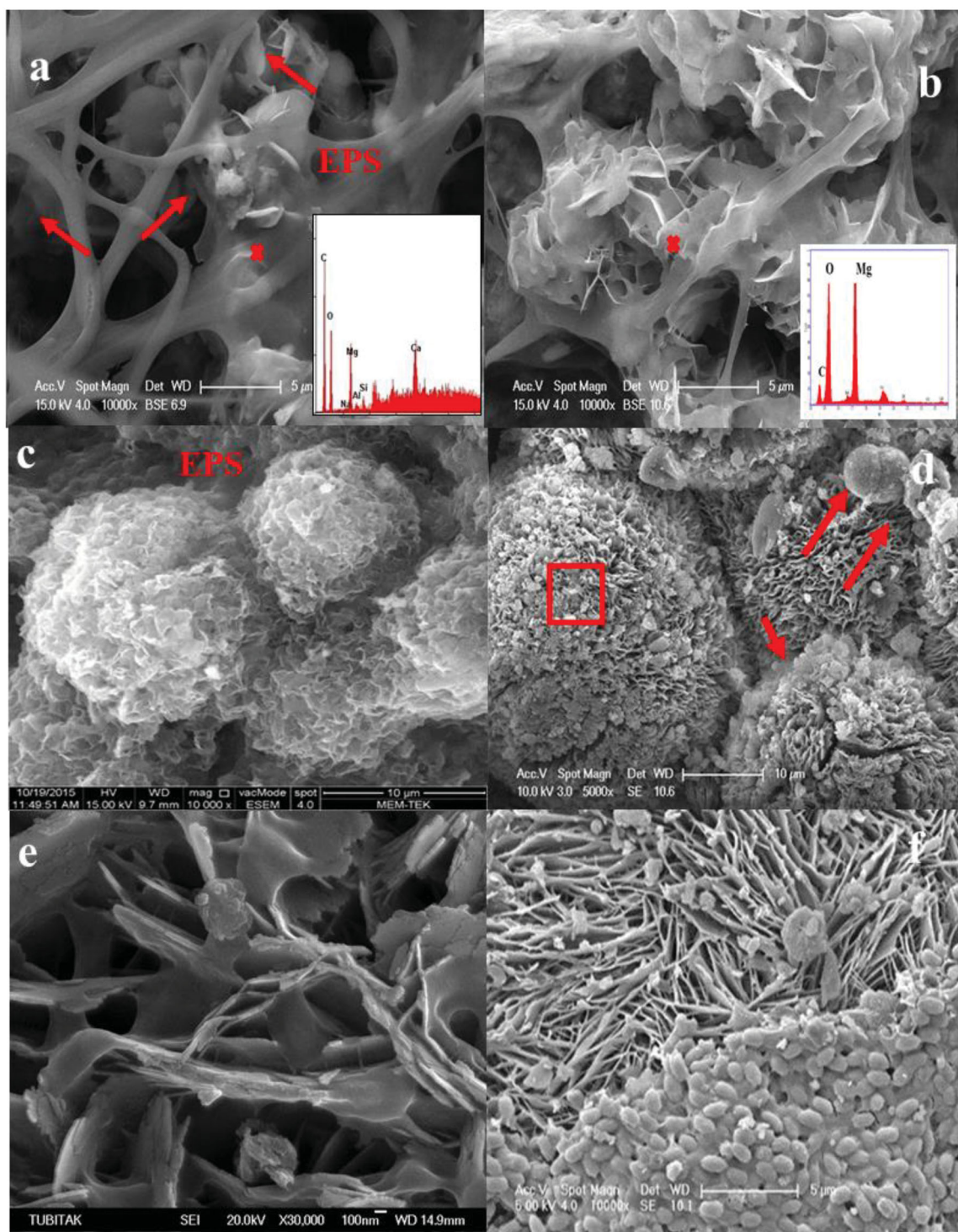
Figure 14. (a) Views of cyanobacterial filaments and plate like hydromagnesite crystal in the mat (SLM2). (b) Widespread occurrences of hydromagnesite crystals on the outer surface of cyanobacterial filaments and EPS (EDX from the cross). (c) Formation of first stage hydromagnesite spheres via aggregation of poorly packet plate like crystals on EPS. (d) Hydromagnesite spheres with tightly packet flakes. (e) A larger view of the square in (d), showing honey comb structure. (f) Hydromagnesite flakes covered by the cells glued by organic matrix.

stromatolites (Figure 11(e)). In future studies, we will assess their diversity, functions and exact roles in the lake.

Microbial community composition of the mat samples implies that precipitation of carbonates, mainly hydromagnesite, in the lake may likely be a net result of metabolic activities of phototrophs and heterotrophs. However, these determinations may carry some uncertainties due to a limited number of mat samples, mostly representing cauliflower and dome shaped stromatolites in the lake. Nevertheless, prevailing occurrences of the cauliflower and dome shaped stromatolites in the lake give confidence that a correlation between microbial diversity of the mats and their metabolic functions may in fact provide valuable insights into stromatolite formation. As indicated by the sequence

data, oxygenic cyanobacteria (*Synechococcus* sp. *Halospirulina, Gloeocapse* sp.), particularly filamentous (*Schizothrix* sp., and *Lyngbya* sp) are dominant microbial cells at top 5 mm of the mats (Figure 11(c,d)). SEM images of this zone (0–5 mm, SLM2-1) revealed that the precipitation is closely associated with the cyanobacteria filaments embedded by EPS (Figure 11(c,f), Figure 14(a,b)). Presence of Mg, Ca and Si on the EPS matrix demonstrated that chemical properties and their functional groups of the EPS provide effective nucleation sites for Mg and Ca ions as previously observed in various microbialites sites (Couradeau et al. 2011; Kazmierczak et al. 2011; Lopez-Garcia et al. 2005; Saghai et al. 2015) (Figure 14(a), EDS spectra). Consistently, a large quantity of acidic functional groups in the EPS (ABM assay) at upper surface implies a high binding capacity of the EPS, particularly calcium, likely leaving Mg more available for precipitation (Figure 7(b)) (Pace et al. 2018). Mineralogical composition of the mat comprised mainly of hydromagnesite further consistent with this (Figure 4). Besides providing nucleation sites, cyanobacteria (e.g., *Schizothrix* sp.) cause pH increase and alkalinity in their microenvironments via their extracellular carbonic anhydrase by dissociating bicarbonate ions into OH and CO_2 and. Later, consumption of CO_2 by photosynthetic microorganisms trigger precipitation of excess Mg in the reactive fluid (Braissant et al. 2009; Kawaguchi and Decho 2002; Reid et al. 2000). In addition to oxygenic photosynthesizers, anoxygenic photosynthetic bacteria (e.g., Chloroflexi) and heterotrophs such as Firmicutes (e.g., *Exiguobacterium*), γ-proteobacteria (*Pseudomonas* and *Rheinheimera* species) identified in the mats may likely contribute to precipitation by increasing alkalinity.

At depths (>10mm) aerobic heterotrophic bacteria may cause pH increase by respiring N rich organic compounds, by product of oxygenic photosynthesis and oxidative deamination (NH_4/NH_3 system) provides pH conditions similar to those found at the surface of the microbial mat during photosynthesis (Hatayama and Saito 2019; Yang et al. 2017). The capacity of heterotrophs to precipitate carbonates (e.g., aragonite, hydromagnesite and dolomite) has been documented by experimental (Balci and Demirel 2016; Rivadeneyra et al. 1999, 2004; Sanchez-Roman et al. 2011) and field studies (Gérard et al. 2013, 2018; Lopez-Garcia et al. 2005; Sanz-Montero et al. 2019).

Consistent with the other natural environments, abundant and diverse heterotrophic bacteria (e.g., Firmicutes) including many Proteobacteria and Firmicutes, identified in the mats, particularly deeper part of the lake highlights important role of heterotrophic bacteria, at least alkaliphilic members of Firmicutes, in formation of microbialites as stated earlier by Sanz-Montero et al. (2019).

Influence of microbial metabolisms on carbonate microfabrics

Hydromagnesite represents up to ca. 92% of the bulk mineralogy of the mat samples (SLM1and SLM2) along with minor amount of aragonite (up to 5%) (Figure 4).

Previously, biologically induced hydromagnesite and aragonite formations are reported in different lacustrine microbialites (Couradeau et al. 2011, 2012; Gérard et al. 2013, 2018; Kazmierczak et al. 2011; Saghai et al. 2015). Morphological observation of the dissected mat sample (SLM2) along with the depth profile of EPS revealed varies types of hydromagnesite microfabrics closely coupled with the degradation of EPS (Figures 6 and 14).

Early incipient hydromagnesite precipitation is particularly widespread and coincided with cyanobacterial rich top mat layer (SLM2-1 section, 0-5 mm) (Figure 2(b,d), Figure 11(b), Figure 14(a,b)). Compared to 5–10 mm of the mat EPS polymers of this layer have relatively less acidic functional groups, providing limited nucleation sites for Mg and Ca ions, as indicated by Alcien Blue content (ABA) of EPS (1.3×10^4 μg/g EPS). Hydromagnesite produced in this top layer consists of mostly plate like crystals growing on EPS (Figure 11(a,b); Figure 14(a–b) and are considered as a product of high photosynthesis with decreasing degree of inhibition.

At depth 5–10 mm where intermixed green and orange mat layer is located (SLM2-2, Figure 11(b)) the amount of acidic functional groups in the EPS increased and scarce hydromagnesite spherulites with 10 and 20 μm in size were formed via aggregation of plate like hydromagnesite crystals (Figure 14(b,c)). These spheres are likely a product of high photosynthesis effect simultaneous to a high inhibition by pristine exopolymers as indicated by their enriched $\delta^{13}C$ values and EPS profile (Figure 13) (Arp et al. 2012). At depth 10–15 mm a sharp decrease in the amount of EPS refers a successive heterotrophic activity leading to formation of hydromagnesite spheres with honeycomb structures (Figure 14(d,e)). Apparently, acidity of the EPS affected the morphology of hydromagnesite (Braissant et al. 2003) and partly degraded EPS likely provided nucleation sites for Mg to promote hydromagnesite precipitation. Similarly, formation of hydromagnesite with honeycomb structure was reported in culture experiments with *Synechococcus* sp. isolated from Lake Salda by Shirokova et al. (2013) and in Lake Eras, an extreme alkaline lake in Spain, by Sanz-Montero et al. (2019). A dumbbell shape mineral, likely dolomite, and some precipitates associated with microbial cells on the surface of these spheres are occasionally observed (Figure 14(d)).

Unlike EPS rich zones grape-like hydromagnesite spherulites, measuring between 2–3 μm, deposit among the plate-like crystals in the EPS-poor layers (SLM2-3, SLM2-4; 15–20 mm) (Figure 6(a–b)). This type microfabric observed only at EPS minimum zone coincided with a high number of heterotrophic bacteria (e.g., Firmicutes, Figure 5). Aggregations of hydromagnesite nanoparticles and bacterial sheaths occasionally covered by nanoglobules are often associated with these small spheres (Figure 6(c–d)). Clusters of plate like hydromagnesite crystals on bacterial cells embedded by EPS produced rosette type morphology (Figure 6(b)). Spherical carbonate nanoglobules tightly associated with cell surfaces of heterotrophic bacteria (e.g., Firmicutes) were identified in the deeper part of the

mat (Figure 6(e), SLM2-4), where the lowest amount of EPS was measured (Figure 7). EDS pattern of these globules and XRD pattern the mat sample (SLM2) revealed Ca and aragonite, respectively (Figure 4, Figure 6(h)). Occurrences of these cell bound aragonite nanoglobules and smaller size hydromagnesite spherulites covered by nanoparticles at the EPS minimum zone are attributed to a heterotrophic decomposition of EPS matrix and thus decreasing degree of inhibition (Braissant et al. 2009; Dupraz et al. 2004; Dupraz and Visscher 2005).

Formation of nanoglobular carbonates, particularly aragonite, have been reported in microbialites (Couradeau et al. 2011; Gérard et al. 2013; Lopez-Garcia et al. 2005; Sanz-Montero et al. 2019). Consistently, various spherulitic carbonates have been shown to precipitate under the influence of organic matter during aerobic heterotrophic activity (Benzerara et al. 2006; Gomez et al. 2018; Krause et al. 2012; Rivadeneyra et al. 1999). Sanz-Montero et al. 2019 attributed the formation of carbonate nanoglobules to declining metabolic activity of heterotrophs due to organic substrate shortage. The same formation mechanism may apply for our case and hydromagnesite and aragonite nanoglobules identified in the EPS-poor zone were likely produced by heterotrophic bacteria as a response to decreasing organic matter.

The lipid composition of living and fossil stromatolites

The lipid distribution reflects the major mat-building microorganisms, as well as the incorporation into the mat system of lipids derived from non-building aquatic and terrestrial organisms. The presence of n-$C_{17:0}$ alkane, 6Me-$C_{17:0}$, 7Me-$C_{17:0}$, n-$C_{19:1}$ alkene and diploptene is indicative of cyanobacterial activity as these compounds are known markers for cyanobacteria (Bauersachs et al. 2017; Coates et al. 2014; Jahnke et al. 2004). They have been found in hypersaline cyanobacterial mats (Jahnke et al. 2004; Scherf and Rullkötter 2009), in freshwater microbial mat constructed by calcifying cyanobacteria (Schizothrix sp.; Thiel et al. 1997), as well as in stromatolites (Allen et al. 2010; Pagès et al. 2014). Diploptene may also originate from methylotrophs (Summons et al. 1994) and sulfate-reducing bacteria (Blumenberg et al. 2006). Both $C_{25:2}$ HBI and stigmasterol are very likely produced by diatoms such as Navicula sp. and Amphora sp., respectively (Kaiser et al. 2016). Phytane is also common in microbial mats (Allen et al. 2010; Jahnke et al. 2008; Slowakiewicz et al. 2016). It may be derived during diagenesis from the phytyl side chain of chlorophyll a or bacteriochlorophyll (Volkman and Maxwell 1986), but also from the phytanyl side chains of ether-linked polar lipids produced by methanogenic (Rowland and Robson 1990; Volkman 1986) and halophilic Archaea (Allen et al. 2010).

iGDGTs, including crenarchaeol (cren) and its isomer (cren') , are produced by Archaea (Schouten et al. 2013) and have been detected previously in microbial mats (Schouten et al. 2007; Slowakiewicz et al. 2016). While cren is considered as specific marker for Thaumarchaeota, iGDGT-0 is most abundant in methanogen Archaea (Schouten et al. 2013). High relative amounts of iGDGT-0 in sample LS1

(Figure 6) likely reflect the high abundance of the methanogen Archaea Methanosphaera (SLM1; Figure 5). Comparatively, the lower percentage of iGDGT-0 and the relatively higher percentage of cren in sample LS2 may reflect the lower relative amount of methanogen Archaea (SLM2). bGDGTs are very likely produced by Acidobacteria (Sinninghe Damsté et al. 2011; Weijers et al. 2006) and were found in hot spring sediments and cyanobacterial mats (Hedlund et al. 2013; Slowakiewicz et al. 2016). bGDGTs may be in situ produced in hot springs by Acidobacteria indigenous to stromatolites, particularly for bGDGT-Ia, Ib, and Ic (Hedlund et al. 2013). Furthermore, bGDGTs might also be produced by bacteria of the phyla Bacteroidetes, Dictyoglomi, and the candidate phylum 'Atribacteria' (Zhang et al. 2013). However, an allochthonous terrestrial source cannot be ruled out since bGDGTs are known to be abundant in soils (Weijers et al. 2006).

Concerning lipids of non-building organisms, n-$C_{27:0}$, n-$C_{29:0}$, and n-$C_{31:0}$ alkanes land plant wax lipids were also found in other microbial mats and stromatolites, and their presence reflects a significant incorporation of terrestrially-derived organic material into the mat system (Allen et al. 2010; Thiel et al. 1997). The main sterols and stanols counterparts (produced by bacterial hydrogenation of sterols) were also found as most abundant steroids in other microbial mats and stromatolites (Allen et al. 2010; Scherf and Rullkötter 2009; Slowakiewicz et al. 2016; Thiel et al. 1997), and are very likely produced by the dinoflagellate Peridinium cinctum in Lake Salda (Kaiser et al. 2016). Although n-$C_{18:0}$ alkanol has been found in cyanobacterial mats and stromatolites (Slowakiewicz et al. 2016), relative amounts of n-$C_{18:0}$, n-$C_{20:0}$, and n-$C_{22:0}$ alkanols as high as in Lake Salda were not observed in other stromatolites so far. Microalgae may represent a direct source for these alkanols (Rezenka et al. 1986).

The distribution of the main stable lipid biomarkers found in Lake Salda living stromatolites seems to reflect part of the bacterial, archaeal and eukaryote communities. Both the microbial and lipid composition suggest two different stromatolite provinces in Lake Salda, one located in the Southwest (S1 site, including SLM1 and SF2 samples) and one located in the east (S2 site, including SLM2, and FS3, FS1 samples). Based on the available dataset, we suggest here that the differences between these two main provinces may related to the geographical and sampling depth where SLM1 and SF1 samples represents upper most part of the living and subfossil stromatolites, respectively (Figures S1 and S2). Importantly, living stromatolites are apparently excellent analogs as the lipids produced by the microbial and eukaryote communities are very similar to those observed from the fossil stromatolites.

Formation mechanisms of stromatolites: insights from the new findings

Formation of Lake Salda stromatolites is solely attributed to cyanobacterial activity by different authors (Braithwaite and Zedef 1994, 1996; Russell et al. 1999; Shirokova et al. 2011, 2013). However, microbial community structure and
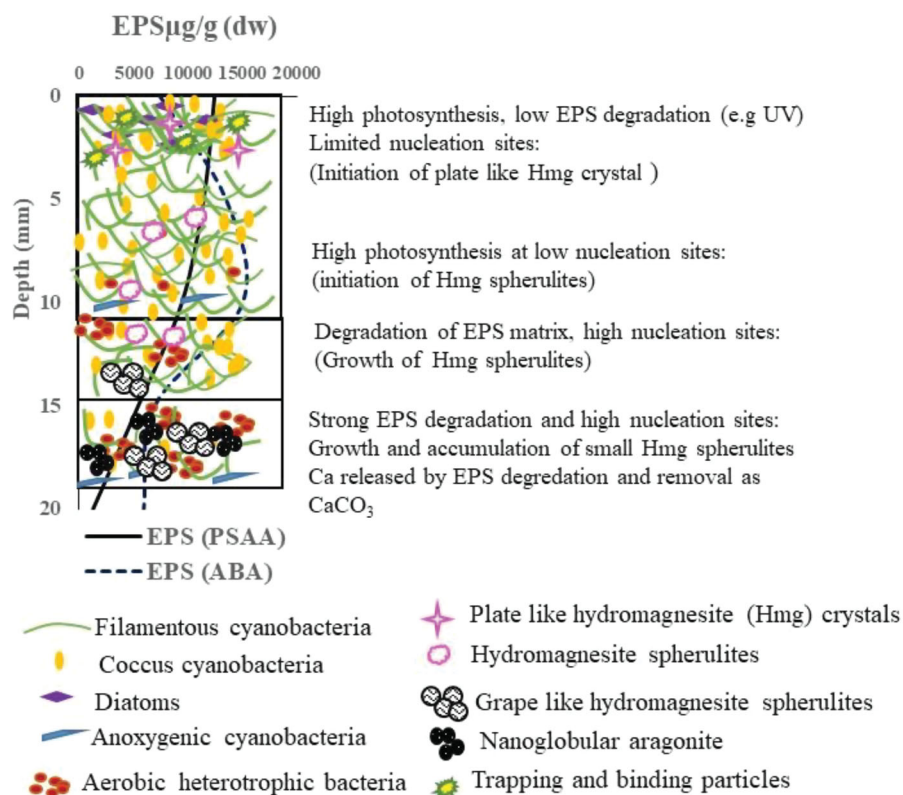
Figure 15. A conceptual model describing Mg and Ca precipitation in the microbial mat.

microscopic observations of the stromatolitic mats suggest that hydromagnesite precipitation is largely controlled by a consortium of cyanobacteria and aerobic heterotrophic bacteria (Figures 5 and 6, Figures 7 and 11, Figure 14). Our results for the first time provide strong evidence for a close association of aerobic heterotrophic bacteria with precipitation of carbonates in Lake Salda stromatolitic mats.

A number of studies have clearly demonstrated the ability of aerobic heterotrophic bacteria to use C and N rich proteinaceous substances produced by cyanobacteria, and that these organisms thus play a significant role in C cycling by regenerating CO_2 required for photosynthesis (Behrens et al. 2008; Ionescu et al. 2015; Pett-Ridge and Weber 2012). Carbonate precipitation in such a consortium would occur if photosynthesis (P) > respiration (R), and if R > P dissolution would take place (Pinckney and Reid 1997). Consequently, hydromagnesite precipitation is likely the result of the net metabolic activities of aerobic heterotrophs and oxygenic photosynthesis regulating CO_2 cycling and pH within the microbial mat. In the lake, activity of this microbial consortium was printed on carbonate mineralogy and textures taking place on the decaying organic matrices (EPS) and bacterial cells in the mats (Figures 6 and 14).

Our results demonstrated that bacterial cells and abundance of EPS and their chemical functional groups (e.g., acidic groups) play a critical role in the lake to overcome kinetically inhibited Mg precipitation as suggested by SI values of the lake water.

Based on depth profile of EPS, microbial community structure and carbonate textures of the mat the following processes likely responsible for carbonate, mainly hydromagnesite, precipitation in the mat: (1) EPS binds Mg and Ca via their functional groups (e.g., acidic functional groups) and kinetically inhibits nucleation and thus precipitation and (2) depth profile of EPS demonstrate a degradation related to increasing aerobic heterotrophic activity (Figure 15). In 10 mm of the mat, cyanobacteria and possibly diatoms colonized the surface of the mat and create carbonate-saturated conditions by consuming CO_2 and thus promote alkalinity and pH increase. However, owing to a large quantity of acidic functional groups in the EPS this layer possesses a high binding Mg and Ca capacity and therefore an immediate precipitation may not occur. Lack of continues lamination and presence of patchy carbonates, hydromagnesite, in the mat zone likely occur as a result of local degradation of EPS providing nucleation sites and due to high Mg/Ca ration in the overlying water. Taking into account that the lake water has low Ca concentration exopolymers binding Ca will even limit or prevent Ca carbonate precipitation at 0–10 mm of the mat (Dupraz et al. 2009) (Table S1). Fluctuation in water level, UV may also contribute to EPS degradation at the upper zone (0–5 mm). It is highly likely that a balance between degradation and continues production of EPS controls precipitation of hydromagnesite by providing nucleation sites to overcome kinetic inhibition at this zone.

As demonstrated by EPS profile increasing degradation of EPS by heterotrophic bacteria occurs in lower part of the mat (15–20 mm), releasing Ca and Mg previously bound to EPS and greatly decrease kinetic inhibition for nucleation

(Braissant et al. 2009; Ionescu et al. 2015). This degradation process may create microenvironments with a relatively high Ca content and finally trigger Ca carbonate mineral precipitation. Grape like hydromagnesite spheres covered by nanoparticles and aragonite nanoglobules closely associated with the cell surfaces likely occur at this stage (Figure 6(a,d,f)). All these processes indicate that partial degradation of EPS is likely a rate-limiting step for hydromagnesite precipitation by creating local nucleation sites and thus allowing precipitation. Discontinues lamination with micropeloidal textures identified in the sub/fossil stromatolites can be attributed to local mineralization of EPS following its degradation (Dupraz et al. 2009) (Figure 12(c,e)).

Several metabolic pathways associated with aerobic heterotrophic bacteria have been reported to contribute to carbonate formation via production of ammonia throughout degradation of N rich organic compounds (e.g., peptone, N-compounds→NH_3+H_2O→NH_4^+ +OH^-), thereby increasing alkalinity, which favors precipitation (Balci et al. 2016; Balci and Demirel 2016; González-López et al. 2005; Rivadeneyra et al. 1999, 2004; Sánchez-Román et al. 2011, 2019). Presence of abundant aerobic heterotrophs (e.g., Firmicutes) in the mats suggest that the same microbial metabolisms likely occur and promote saturation conditions required for the precipitation of carbonates in the mat layers (Cabestrero and Sanz-Montero 2018). Consistently, the formation of Mg carbonates (e.g., hydromagnesite and dolomite nanoglobules) on decayed EPS closely associated with heterotrophs are reported in alkaline lakes (Alcántara-Hernández et al. 2017). Similar to Lake Salda, Mg carbonate precipitation (e.g., hydromagnesite, dolomite nanoglobules) regulated by heterotrophic degradation of organic matrix (e.g., EPS) in an evaporative and ephemeral alkaline Lake Eras has been recently documented by Sanz-Montero et al. (2019). The general microbial community, carbonate mineralogy and textures of Lake Salda mats are comparable to other microbialites independently of physicochemical conditions such as water salinity, content, temperature or pH (Gérard et al. 2013, 2018; Salvatore et al. 2018; Sanz-Montero et al. 2019). These similarities within the microbial populations and carbonate mineralogy suggest that metabolic activities and environmental interactions may be more critical than taxonomic diversity and that a diverse range of metabolisms, rather than cyanobacteria, may have been likely involved in stromatolite formations preserved in the geological records.

The lack of co-variance among $\delta^{13}C_{carb}$ and $\delta^{18}O_{carb}$ values and the enrichment in $\delta^{13}C_{carb}$ values of the bulk carbonate (92–95% hydromagnesite) of the living stromatolites indicate that ^{13}C preferentially enriched in hydromagnesite (Figure 13). High carbonate $\delta^{13}C$ values measured in different microbialites (e.g., Pavillion, average +2.31‰; Great Salt Lakes,) are generally attributed to photosynthetic uptake of $^{12}CO_2$ leaving isotopically heavy carbon for precipitation (Chagas et al. 2016, and references therein) whereas carbonates with negative $\delta^{13}C$ values are considered to reflect heterotrophic activity producing carbon source with low $\delta^{13}C_{DIC}$ values such as sulfate reduction (Neuweiler et al. 1997) and oxidative biodegradation. Our results

demonstrated that the precipitation in the stromatolitic mats was associated with coupled processes of photosynthetic and aerobic heterotrophic activity. Although it was not possible to quantitatively determine contribution of each metabolic pathway to $\delta^{13}C_{DIC}$ values of lake water, high $\delta^{13}C$ values of the hydromagnesite refer to photosynthetic activity as a primary producer for carbonate mineral saturation in the lake. In contrast to hydromagnesite occurrences close association of aragonites with bacteria surface demonstrated that aragonite is likely a product of heterotrophic activity occurring in the mat. However, low percentages of aragonite (3–6%) in the bulk carbonate hinder $\delta^{13}C$ values of aragonite pronounced on the bulk carbonate due to its low mass (Balci et al. 2007).

Hydromagnesite precipitation in the lake likely occurs as the lake water is subject to evaporation as indicated by the high $\delta^{18}O_{LW}$values (+4‰) of lake water relative to $\delta^{18}O_{GW}$ values (−8‰) of groundwater. The high $\delta^{18}O_{carb}$ values identified in this study are in good agreement to the $\delta^{18}O$ range reported for Lake Salda (Braithwaite and Zedef 1996) and hydromagnesite rich carbonates closely associated with microbial mats in lacustrine lakes (Power et al. 2007; Sanz-Montero et al. 2019).

A good correlation exists between $\delta^{13}C$ values of the living and fossil stromatolites suggest that the fossil stromatolites may have been mineralized in similar water chemistry under the influence of similar microbial interactions to those currently occurring in the lake, at least for the last 750 years.

Biosignature preservation potential of Lake Salda stromatolites

Hydromagnesite formation has been reported in a range of geologically different settings (Gérard et al. 2013; Kazmierczak et al. 2011; Power et al. 2009; Sanz-Montero et al. 2013, 2019). However, the persistence of hydromagnesite microbialites and their long-term stability is questionable (Russell et al. 1999). For Lake Salda stromatolites, Russel et al. (1999) argued that hydromagnesite stromatolites degenerate soon after their formation to porous, poorly lithified rocks, and their subsequent diagenetic alteration to magnesite might lower biosignature preservation potential of the stromatolites. However, these suggestions are largely based on the macro-scale morphological features of the stromatolites. In contrast, we find that the mineralogical composition of the fossil stromatolites shows the persistence of hydromagnesite at least for the last 750 years. Consistent with our results, preservation of microfabrics and morphologies of Miocene aged magnesitic microbialites and presence of 2.8 ka BP aged microbially induced hydromagnesite in Lake Alchichica (Puebla, Mexico) gives further evidence of biosignature integrity of Mg-rich microbialites (Kazmierczak et al. 2011; Sanz-Montero and Rodríguez-Aranda 2012).

Petrographic observations of the mats clearly revealed hydromagnesite precipitation in cyanobacterial sheaths and EPS with various textures including spherical ones formed by clusters of plate-like crystals showing the honeycomb-like

structure, nanosize particles, and spheres (Figures 6 and 14). Wavy laminated textures composed of alternating clotted peloidal and/or aphanitic micrite and silt-sized peloids, with rare hollow spheroids preserved in the sub/fossil stromatolite are comparable with those recorded in the microbial mat indicating comparable precipitation processes (Figure 11(f), Figure 12(a–d)). As in their modern counterparts, the fossil hydromagnesites clearly show well-preserved cyanobacterial filaments, coccoid and spherical structures closely associated with micropeloids (Figure 12(c–e,g,h)).

Columnar structures with pure laminates observed in the sub/fossil stromatolite resemble the mini columnar structure of the living stromatolites (Figure S1(g,h), Figure S2(d–f)). The clotted micropeloidal structures in the sub/fossil stromatolites are often considered as remnants of coccoid clusters or filamentous bacteria, which discontinuously mineralized in the presence of EPS as observed in upper layer of the mat (Figure 11(e,f), Figure 15) (Chafetz 1986; Dupraz et al. 2009). As for the living stromatolites, the weak or non-lamination with an extremely irregular thickness and no lateral persistence in the sub/fossil stromatolites may arise from the high EPS production and its subsequent decomposition by microbial cells (Figure 12(b,c)). Decho et al. (2005) suggested that a high-continued production of EPS by photosynthetic microorganisms may cause the formation of spongy and gelatinous stromatolitic mats with a weak or no lithification since much of Ca or Mg would be bound, making fewer ions available for continues precipitation (Figure 11(a,b)). The thin needle-like aragonite crystals occurring around intra-clasts may be comparable with nano-size aragonite observed in the microbial mat (Figure 6(f), Figure 12(f)) (Visscher et al. 1998). In fact, the formation of needle-like carbonate crystals evolved from either carbonate nanograins (aragonite) or from a euhedral shape crystal (calcite) in an organic matrix (e.g., EPS, amino acids) may refer their biosignatures preservation potential (Braissant et al. 2003; Kremer et al. 2012). Furthermore, the lipid distribution, which reflects the main mat-building microorganisms, is strikingly similar in the living stromatolitic mat and fossil stromatolites (Figures 8–10). The lipid composition of fossil stromatolites can thus be used to trace faithfully the distribution of mat-building microorganisms in the past, at least for Lake Salda.

These results have direct implications for the search for biosignatures on Mars. NASA's Mars 2020 rover is tasked with searching for signs of ancient microbial life on Mars and collecting samples for eventual sample return to Earth. In 2021, the rover will land in Jezero crater, which is a 45 km diameter crater on the rim of the Isidis Basin. Jezero was chosen as the landing site for the mission based on the combination of a well-preserved delta, indicating a long-lived paleolake with both inlet and outlet channels, as well as excellent access to regional ultramafic carbonate-bearing units in the crater (e.g., Fassett and Head 2005; Goudge et al. 2017, 2018). The watershed of Jezero cuts through these units as well as other older ultramafic terrains (Goudge et al. 2015). In addition, some of the carbonate deposits in the crater may have been produced or altered by lacustrine near-shore carbonate precipitation similar to Lake Salda. These deposits are located along the crater margins, at elevations consistent with paleoshorelines, and exhibit visible/near-infrared spectral signatures from orbit consistent with hydrated Mg-carbonate (Horgan et al. 2019). These minerals have been proposed to result from diagenetic transformation of primary hydromagnesite precipitates in the Jezero paleolake. Based on the results of this study, these deposits could possibly preserve microbial biosignatures that would be detectable in returned samples, as well as sub-mm textures providing constraints on their origin that could be detectable by the highest resolution imagers on the rover

Conclusions

By combining microscopic observations along with microbial diversity, lipid, inorganic geochemical and stable isotope analysis, this study reveals that at least two different metabolic pathways (aerobic respiration and photosynthesis) contribute to stromatolite formation in Lake Salda. Influences of microbial metabolisms are recorded into the texture of hydromagnesite and aragonite precipitated in the mats. In the uppermost part of the stromatolitic mats, photosynthetic microbial cells play a critical role by excreting a well-developed EPS matrix and hydromagnesite precipitation occurs on the EPS matrix serving as a template to initiate mineral precipitation upon its degradation. At this EPS rich zone, hydromagnesite nucleates first on EPS and, poorly tight plate-like crystal clusters developed and subsequently evolved into larger tightly packed spheres. With decreasing organic matter due to heterotrophic activity at the lower part of the mat, relatively small-sized, grape-like hydromagnesite spheres covered by even hydromagnesite nanoparticles and nanoglobules develop and do not show plate-like crystal considered typical for hydromagnesite mineral. Aragonite nanoglobules closely associated with the microbial cell surfaces are only identified at the mat zone with the lowest amount of EPS suggesting a critical role for EPS in the precipitation. ^{13}C-enriched carbon isotope signatures of hydromagnesite clearly imply photosynthesis as primary producers for carbonate saturation in the lake while microfabrics of hydromagnesite refer to EPS degradation as a triggering precipitation mechanism in Lake Salda mats. This EPS regulated hydromagnesite precipitation should provide good evidence for organomineralization processes. Therefore, discrete, irregular discontinues laminae with clotted, micro/peloidal microfabrics in the fossil stromatolites may be considered to result from carbonate precipitation occurring on organic matrix produced by biological activity. Similarities in lipid profiles, crystal morphologies and $^{13}\delta$C values of the modern and fossil stromatolites as well as preserved cyanobacterial cells provide strong evidence that hydromagnesite may be considered as a good preservation agent for biosignatures in Lake Salda.

Disclosure statement

References

Akçer-Ön S, Bora Ön Z, Çağatay MN, ERiş KK, Sakınç M, Wulf S, Helvacı C, Acar D, Gündoğan İ, Akkiraz S, et al. 2016. High resolution Middle-Late Holocene climatic records from Lake Salda (W. Anatolia) Sediments. Proceedings of MedCLIVAR 2016 Conference, Athens, Greece.

Alcántara-Hernández RJ., Valdespino PM, Centeno CM, Alcocer J, Merino-Ibarra M, Falcón LI. 2017. Genetic diversity associated to N cycle pathways in microbialites from Lake Alchichica, Mexico. Aquat Microb Ecol 78(2):121–133.

Allen MA, Neilan BA, Burns BP, Jahnke LL, Summons RE. 2010. Lipid biomarkers in Hamelin Pool microbial mats and stromatolites. Org Geochem 41(11):1207–1218.

Allwood AC, Walter MR, Kamber BS, Marshall CP, Burch IW. 2006. Stromatolite reef from the Early Archaean era of Australia. Nature 441(7094):714–718.

Altermann W, Kazmierczak J, Oren A, Wright D. 2006. Microbial calcification and its impact on the sedimentary rock record during 3.5 billion years of Earth history. Geobiology 4(3):147–166.

Arp G, Helms G, Karlinska K, Schumann G, Reimer A, Reitner J, Trichet J. 2012. Photosynthesis versus exopolymer degradation in the formation of microbialites on the atoll of Kiritimati, Republic of Kiribati, Central Pacific. Geomicrobiol J 29(1):29–65.

Awramik SM, Buchheim HP. 2009. A giant, Late Archean lake system: the Meentheena Member (Tumbiana Formation; Fortescue Group), Western Australia. Precambrian Res 174(3–4):215–240.

Awramik SM, Buchheim HP. 2015. Giant stromatolites of the Eocene Green River Formation (Colorado, USA). Geology 43(8):691–694.

Awramik SM, Grey K. 2005. Stromatolites: biogenicity, biosignatures, and bioconfusion. Paper presented at: Proceedings of SPIE, San Diego, CA.

Balci N, Demirel C. 2016. Formation of carbonate nanoglobules by a mixed natural culture under hypersaline conditions. Minerals 6(4):122.

Balci N, Demirel C, Akcer-On S, Gültekin AH, Kurt MA. 2018. Evaluating abiotic and microbial factors on carbonate precipitation in Lake Acıgöl, a hypersaline lake in Southwestern Turkey. Quaternary Int 486:116–128.

Balci N, Menekse M, Karagüler N, Sönmez MS, Meister P. 2016. Reproducing authigenic carbonate precipitation in the hypersaline Lake Acıgöl (Turkey) with microbial cultures. Geomicrobiol J 33(9):758–773.

Balci N, Shanks WC, Mayer B, Mandernack KW. 2007. Oxygen and sulfur isotope systematics of sulfate produced by bacterial and abiotic oxidation of pyrite. Geochim Cosmochim Acta 71(15):3796–3811.

Batchelor M, Burne R, Henry B, Slatyer T. 2005. Statistical physics and stromatolite growth: new perspectives on an ancient dilemma. J Phys A 35:6–11.

Bauersachs T, Talbot HM, Sidgwick F, Sivonen K, Schwark L. 2017. Lipid biomarker signatures as tracers for harmful cyanobacterial blooms in the Baltic Sea. PLoS One 12(10):e0186360.

Behrens S, Losekann T, Pett-Ridge J, Weber PK, Ng W-O, Stevenson BS, Hutcheon ID, Relman DA, Spormann AM. 2008. Linking microbial phylogeny to metabolic activity at the single-cell level by using enhanced element labeling-catalyzed reporter deposition fluorescence in situ hybridization (EL-FISH) and NanoSIMS. Appl Environ Microb 74(10):3143–3150.

Benzerara K, Menguy N, LóPez-Garcia P, Yoon T-H, Kazmierczak J, Tyliszczak T, Guyot F, Brown EJ. Jr. 2006. Nanoscale detection of organic signatures in carbonate microbialites. Proc Natl Acad Sci, USA 103(25):9440–9445.

Bergmann J, Friedel P, Kleeberg R. 1998. BGMN a new fundamental parameter based Rietveld program for laboratory X-ray sources, its use in quantitative analysis and structure investigations. Commission of Powder Diffraction. Int Union Crystallogr 20:58.

Blumenberg M, Nauhaus K, Oppermann BI, Pape T, Krüger M, Talbot HM, Michaelis W. 2006. Biosynthesis of hopanoids by sulfate-reducing bacteria (genus Desulfovibrio). Environ Microbiol 8:1220–1227.

Bober C, Mojica K, Cooney M. 2005. Quantification of single-species marine biofilm with alcian blue. J Young Investigat 12:1–4.

Bosak T, Greene S, Newman DK. 2007. A likely role for anoxygenic photosynthetic microbes in the formationof ancient stromatolites. Geobiology 5(2):119–126.

Braissant O, Cailleau G, Dupraz C, Verrecchia EP. 2003. Bacterially induced mineralization of calcium carbonate in terrestrial environments: the role of exopolysaccharides and amino acids. J Sediment Res 73:485–490.

Braissant O, Decho AW, Dupraz C, Glunk C, Przekop KM, Visscher PT. 2007. Exopolymeric substances of sulfate-reducing bacteria: interactions with calcium at alkaline pH and implication for formation of carbonate minerals. Geobiology 5(4):401–411.

Braissant O, Decho AW, Przekop KM, Gallagher KL, Glunk C, Dupraz C, Visscher PT. 2009. Characteristics and turn over of exopolymeric substances in a hypersaline microbial mat. FEMS Microbiol 67(2):293–307.

Braithwaite CJR, Zedef V. 1996. Hydromagnesite stromatolites and sediments in an alkaline lake, Salda Golu, Turkey. J Sedimentary Res 66:91–1002.

Cabestrero O, Sanz-Montero ME. 2018. Brine evolution in two inland evaporative environments: influence of microbial mats in mineral precipitation. J Paleolimnol 59(2):139–157.

Çağatay MN, Wulf S, Sancar Ü, Özmaral A, Vidal L, Henry P, Appelt O, Gasperini L. 2015. The tephra record from the Sea of Marmara for the last ca. 70 ka and its palaeoceanographic implications. Mar Geol 361:96–110.

Casaburi G, Duscher AA, Reid RP, Foster JS. 2016. Characterization of the stromatolite microbiome from Little Darby Island, The Bahamas using predictive and whole shotgun metagenomic analysis. Environ Microbiol 18:1452–1469.

Chafetz HS. 1986. Marine peloids: a product of bacterially induced precipitation of calcite. J Sed Petrol 56:812–817.

Chagas AP, Webb GE, Burne RV, Southam G. 2016. Modern lacustrine microbialites: towards a synthesis of aqueous and carbonate geochemistry and mineralogy. Earth-Sci Rev 162:338–363.

Coates RC, Podell S, Korobeynikov A, Lapidus A, Pevzner P, Sherman DH, Allen EE, Gerwick L, Gerwick WH. 2014. Characterization of cyanobacterial hydrocarbon composition and distribution of biosynthetic pathways. PLoS One 9(1):e85140.

Coplen TB, Kendall C, Hopple J. 1983. Comparison of stable isotope reference. Nature 302(5905):236–238.

Corsetti FA, Storrie-Lombardi MC. 2003. Lossless compression of stromatolite images: a biogenicity index? Astrobiology 3(4):649–655.

Couradeau E, Benzerara K, Gérard E, Estève I., Moreira D, Tavera R, López-García P. 2013. Cyanobacterial calcification in modern microbialites at the submicrometer scale. Biogeosciences 10:5255–5256.

Couradeau E, Benzerara K, Moreira D, Gérard E, Kazmierczak J, Tavera R, López-García P. 2011. Prokaryotic and eukaryotic community structure in field and cultivated microbialites from the alkaline lake of Alchichica, Mexico. PloS ONE 6:e28767.

Decho AW, Kawaguchi T, Allison MA, Louchard EM, Reid RP, Stephens FC, Voss KJ, Wheatcroft RA, Taylor BB. 2003. Sediment properties influencing upwelling spectral reflectance signatures: the 'biofilm gel effect'. Limnol Oceanogr 48(1):431–443.

Decho AW, Visscher PT, Reid RP. 2005. Production and cycling of natural microbial exopolymers (EPS) within a marine stromatolithe. Palaeogeogr Palaeoclimatol Palaeoecol 219(1–2):71–86.

DeSantis TZ, Hugenholtz P, Larsen N, Rojas M, Brodie EL, Keller K, Huber T, Dalevi D, Hu P, Andersen GL. 2006. Greengenes, a

chimera-checked 16S rRNA gene database and workbench compatible with ARB. Appl Env Microbiol 72(7):5069–5072.

DuBois M, Gilles KA, Hamilton JK, Rebers PA, Smith F. 1956. Colorimetric method for determination of sugars and related substances. Anal Chem 28(3):350–356.

Dupraz C, Visscher PT, Baumgartner LK, Reid RP. 2004. Microbe–mineral interactions: early carbonate precipitation in a hypersaline lake (Eleuthera Island, Bahamas). Sedimentology 51: 745–765.

Dupraz C, Reid RP, Braissant O, Decho AW, Norman RS, Visscher PT. 2009. Processes of carbonate precipitation in modern microbial mats. Earth-Sci Rev 96(3):141–162.

Dupraz C, Visscher PT. 2005. Microbial lithification in marine stromatolites and hypersaline mats. Trends Microbiol 13(9):429–438.

Edgar RC, Haas BJ, Clemente JC, Quince C, Knight R. 2011. UCHIME improves sensitivity and speed of chimera detection. Bioinformatics 27(16):2194–2200.

Fassett CI, Head JW. 2005. Fluvial sedimentary deposits on Mars: ancient deltas in a crater lake in the Nili Fossae region. J Geophys Res 32(14):L14201.

Frantz CM, Petryshyn VA, Corsetti FA. 2015. Grain trapping and binding by filamentous cyanobacterial and algal mats: implications for stromatolite micro-fabrics through time. Geobiology 13(5):409–423.

Garczynski B, Horgan B, Kah LC, Balci N, Gunes Y. 2019. Searching for potential biosignatures in Jezero Crater with Mars 2020. A Vnir spectral investigation of terrestrial lacustrine carbonate analogs. Paper presented at Lunar and Planetary Science Conference, Texas.

Gérard E, De Goeyse S, Hugoni M, Agogué H, Richard L, Milesi V, Guyot F, Lecourt L, Borensztajn S, Joseph M-B, et al. 2018. Key role of alphaproteobacteria and cyanobacteria in the formation of stromatolites of Lake Dziani Dzaha (Mayotte, Western Indian Ocean). Front Microbiol 9:1–20

Gérard E, Ménez B, Couradeau E, Moreira D, Benzerara K, Tavera R, López-García P. 2013. Specific carbonate-microbe interactions in the modern microbialites of Lake Alchichica (Mexico). Isme J 7(10): 1997–2009.

Goh F, Allen MA, Leuko S, Kawaguchi T, Decho AW, Burns BP, Neilan BA. 2009. Determining the specific microbial populations and their spatial distribution within the stromatolite ecosystem of Shark Bay. Isme J 3(4):383–396.

Gomez FJ, Mlewski C, Boidi FJ, Farias M, Gerard E. 2018. Calcium carbonate precipitation in diatom-rich microbial mats: the laguna negra hypersaline lake, Catamarca, Argentina. J Sedimentary Res 88(6):727–742.

González-López J, Rodelas B, Pozo C, Salmerón-López V, Martínez-Toledo MV, Salmerón V. 2005. Liberation of amino acids by heterotrophic nitrogen fixing bacteria. Amino Acids 28(4):363–367.

Goudge TA, Aureli KL, Head JW, Fassett CI, Mustard JF. 2015. Classification and analysis of candidate impact crater-hosted closed-basin lakes on Mars. Icarus 260:346–336.

Goudge TA, Mohrig D, Cardenas BT, Hughes CM, Fassett CI. 2018. Stratigraphy and paleohydrology of delta channel deposits, Jezero crater, Mars. Icarus 301:58–75.

Goudge TA, Milliken RE, Head JW, Mustard JF, Fassett CI. 2017. Sedimentological evidence for a deltaic origin of the western fan deposit in Jezero crater, Mars and implications for future exploration. Earth Planet Sci Lett 458:357–365.

Grotzinger JP, Knoll AH. 1999. Stromatolites in Precambrian carbonates: evolutionary mileposts or environmental dipsticks? Annu Rev Earth Planet Sci 27(1):313–358.

Grotzinger JP, Rothman DH. 1996. An abiotic model for stromatolite morphogenesis. Nature. 383(6599):423–425.

Haas BJ, Gevers D, Earl AM, Feldgarden M, Ward DV, Giannoukos G, Ciulla D, Tabbaa D, Highlander SK, Sodergren E, et al. 2011. Chimeric 16S rRNA sequence formation and detection in Sanger and 454-pyrosequenced PCR amplicons. Genome Res 21(3):494–504.

Hänchen M, Prigiobbe V, Baciocchi R, Mazzotti M. 2008. Precipitation in the Mg-carbonate system: effects of temperature and CO_2 pressure. Chem Eng Sci 63(4):1012–1028.

Hatayama K, Saito K. 2019. Calcite formation induced by Ensifer adhaerens, Microbacterium testaceum, Paeniglutamicibacter kerguelensis, Pseudomonas protegens and Rheinheimera texasensis. Antonie Van Leeuwenhoek 112:711–721.

Hedlund BP, Paraiso JJ, Williams AJ, Huang Q, Wei Y, Dijkstra P, Hungate BA, Dong H, Zhang CL. 2013. Wide distribution of autochthonous branched glycerol dialkyl glycerol tetraethers (bGDGTs) in U.S. Great Basin hot springs. Front Microbiol 4:222.

Hillier S. 2000. Accurate quantitative analysis of clay and other minerals in sandstones by XRD: comparison of a Rietveld and a reference intensity ratio (RIR) method and the importance of sample preparation. Clay Miner 35(1):291–302.

Hofmann HJ, Grey K, Hickman AH, Thorpe RI. 1999. Origin of 3.45 Ga coniform stromatolites in Warrawoona Group, Western Australia. Geologic Soc Am Bull 111(8):1256–1262.

Hopmans EC, Schouten S, Sinninghe Damsté JS. 2016. The effect of improved chromatography on GDGT-based palaeoproxies. Org Geochem 93:1–6.

Horgan B, Anderson R, Dromart G, Amador E, Rice M. 2019. The mineral diversity of Jezero crater: evidence for possible lacustrine carbonates. Icarus: 339 113526.

Ionescu D, Spitzer S, Reimer A, Schneider D, Daniel R, Reitner J, de Beer D, Arp G. 2015. Calcium dynamics in microbialite-forming exopolymer-rich mats on the atoll of Kiritimati, Republic of Kiribati, Central Pacific. Geobiology 13(2):170–180.

Jahnke LL, Embaye T, Hope J, Turk KE, van Zuilen M, Des Marais DJ, Farmer JD, Summons RE. 2004. Lipid biomarker and carbon isotopic signatures for stromatolite-forming, microbial mat communities and Phormidium cultures from Yellowstone National Park. Geobiology 2(1):31–47.

Jahnke LL, Orphan VJ, Embaye T, Turk KA, Kubo MD, Summons RE, Des Marais DJ. 2008. Lipid biomarker and phylogenetic analyses to reveal archaeal biodiversity and distribution in hypersaline microbial mat and underlying sediment. Geobiology 6(4):394–410.

Jogi PM, Runegar B. 2005. Quantitative methods for evaluating the biogenecity of fossil stromatolites. Astrobiology 5:293.

Kaiser J, Belt ST, Tomczak M, Brown TA, Wasmund N, Arz HW. 2016. C25 highly branched isoprenoid alkenes in the Baltic Sea produced by the marine planktonic diatom Pseudosolenia calcar-avis. Org Geochem 93:51–58.

Kaiser J, Ön B, Arz HW, Akcer-Ön S. 2016. Sedimentary lipid biomarkers in the magnesium rich and highly alkaline Lake Salda. J Limnol 75:581–596.

Kawaguchi T, Decho AW. 2002. A laboratory investigation of cyanobacterial extracellular polymeric secretions (EPS) in influencing $CaCO_3$ polymorphism. J Cryst Growth 240(1–2):230–235.

Kazanci N, Girgin S, Dügel M. 2004. On the limnology of Salda Lake, a large and deep soda lake in southwestern Turkey: future management proposals, aquatic conservation. Aquatic Conserv: Mar Freshw Ecosyst 14(2):151–162.

Kazmierczak J, Kempe S, Kremer B, Lopez-Garcia P, Moreira D, Tavera R. 2011. Hydrochemistry and microbialites of the alkaline crater lake Alchichica, Mexico. Facies 57:543–570.

Kempe S, Kazmierczak J. 2007. Hydrochemical key to the genesis of calcareous nonlaminated and laminated cyanobacterial microbialites. In: Seckbach J., editors. Algae and Cyanobacteria in Extreme Environments. Cellular Origin, Life in Extreme Habitats and Astrobiology, Dordrecht, Springer, 11:242–264.

Klock J-H, Wieland A, Seifert R, Michaelis W. 2007. Extracellular polymeric substances (EPS) from cyanobacterial mats: characterization and isolation method optimization. Mar Biol 152(5):1077–1085.

Knoll A. 2003. Biomineralization and Evolutionary History. Rev Mineralogy Geochem 54(1):329–356.

Krause S, Liebetrau V, Gorb S, Sánchez-Román M, McKenzie JA, Treude T. 2012. Microbial nucleation of Mg-rich dolomite in exopolymeric substances under anoxic modern sea water salinity: new insight into an old enigma. Geology 40(7):587–590.

Kremer B, Kazmierczak J, Łukomska-Kowalczyk M, Kempe S. 2012. Calcification and silicification: fossilization potential of

cyanobacteria from stromatolites of Niuafoou's Caldera Lakes (Tonga) and implications for the early fossil record. Astrobiology 12(6):535–548.

López-García P, Kaźmierczak J, Benzerara K, Kempe S, Guyot F, Moreira D. 2005. Bacterial diversity and carbonate precipitation in the giant microbialites from the highly alkaline Lake Van, Turkey. Extremophiles 9:263–274.

Mavromatis V, Bundeleva IA, Shirokova LS, Millo C, Pokrovsky OS, Bénézeth P, Ader M, Oelkers EH. 2015. The continuous re-equilibration of carbon isotope compositions of hydrous Mg carbonates in the presence of cyanobacteria. Chem Geol 404:41–51.

Neuweiler F, Reitner J, Monty C, Feldmann M, Awramik S, Bourque PA, Cirilli S, Gautret P, Marcoux J, Plaziat JC, et al. 1997. Biosedimentology of microbial buildups IGCP project no. 380 Proceedings of 2nd Meeting, Göttingen/Germany 1996. Facies 36(1):195–284.

Pace A, Bourillot R, Bouton A, Vennin E, Braissant O, Dupraz C, Duteil T, Bundeleva I, Patrier P, Galaup S, et al. 2018. Formation of stromatolite lamina at the interface of oxygenic–anoxygenic photosynthesis. Geobiology 16(4):378–398.

Pagès A., Grice K, Vacher M, Welsh DT, Teasdale PR, Bennett WW, Greenwood P. 2014. Microbial communities and processes in a modern stromatolite. Environ Microbiol 16:2458–2474.

Parkhurst D, Appelo CAJ. 1999. User's Guide to PhreeqC (Version 2)—A Computer Program for Speciation, Batch-Reaction, One-Dimensional Transport, and Inverse Geochemical Calculations. Denver, CO: U.S. Department of the Interior.

Passow U, Alldredge AL. 1995. A dye-binding assay for the spectrophotometric measurement of transparent exopolymer particles (TEP). Limnol Oceanogr 40(7):1326–1335.

Pett-Ridge J, Weber PK. 2012. NanoSIP: NanoSIMS applications for microbial biology. Meth Mol Biol 881:375–408.

Pinckney JL, Reid RP. 1997. Productivity and community composition of stromatolitic microbial mats in the Exuma Cays. Bahamas Facies 36:204–207.

Power IM, Wilson SA, Thom JM, Dipple GM, Gabites JE, Southam G. 2009. The hydromagnesite playas of Atlin, British Columbia, Canada: a biogeochemical model for CO_2 sequestration. Chem Geol 260(3–4):286–300.

Power IM, Wilson SA, Thom JM, Dipple GM, Southam G. 2007. Biologically induced mineralization of dypingite by cyanobacteria from an alkaline wetland near Atlin, British Columbia, Canada. Geochem Trans 8:13.

Reid RP, James NP, Macintyre IG, Dupraz CP, Burne RV. 2003. Shark Bay stromatolites: microfabrics and reinterpretation of origins. Facies 49:299–324.

Reid RP, Visscher PT, Decho AW, Stolz JF, Bebout BM, Dupraz C, Macintyre IG, Paerl HW, Pinckney JL, Prufert-Bebout L, et al. 2000. The role of microbes in accretion, lamination and early lithification of modern marine stromatolites. Nature 406(6799):989–992.

Reimer PJ, Bard E, Bayliss A, Beck JW, Blackwell PG, Ramsey CB, Buck CE, Cheng H, Edwards RL, Friedrich M, et al. 2013. Intcal13 and marine13 radiocarbon age calibration curves 0–50,000 years cal bp. Radiocarbon 55(4):1869–1887.

Riding R. 2006. Cyanobacterial calcification, carbon dioxide concentrating mechanisms, and Proterozoic–Cambrian changes in atmospheric composition. Geobiology 4(4):299–316.

Rivadeneyra MA, Delgado G, Soriano M, Ramos-Cormenzana A, Delgado R. 1999. Biomineralization of carbonates by Marinococcus albus and Marinococcus halophilus isolated from Salar de Atacame (Chile). Curr Microbiol 39(1):53–57.

Rivadeneyra MA, Párraga J, Delgado R, Ramos-Cormenzana A, Delgado G. 2004. Biomineralization of carbonates by Halobacillus trueperi in solid and liquid media with different salinities. FEMS Microbiol Ecol 48(1):39–46.

Rowland SJ, Robson JN. 1990. The widespread occurrence of highly branched a cyclic C20, C25 and C30 hydrocarbons in recent sediments and biota - A review. Mar Environ Res 30(3):191–216.

Russell MJ, Ingham JK, Zedef V, Maktav D, Sunar F, Hall AJ, Fallick AE. 1999. Search for signs of ancient life on Mars: expectations

from hydromagnesite microbialites, Salda Lake, Turkey. J Geol Soc 156(5):869–888.

Saghai A, Zivanovic Y, Zeyen N, Moreira D, Benzerara K, Deschamps P. 2015. Metagenome-based diversity analyses suggest a significant contribution of non-cyanobacterial lineages to carbonate precipitation in modern microbialites. Front Microbiol 6:797.

Salvatore MR, Goudge TA, Bramble MS, Edwards CS, Bandfield JL, Amador ES, Mustard JF, Christensen PR. 2018. Bulk mineralogy of the NE Syrtis and Jezero crater regions of Mars derived through thermal infrared spectral analyses. Icarus 301:76–96.

Sánchez-Román M, Romanek CS, Fernandez-Remolar DC, Sanchez-Navas A, McKenzie JA, Pibernat RA, Vasconcelos C. 2011. Aerobic biomineralization of Mg-Rich carbonates: implications for natural environments. Chem Geol 281:143–150.

Sanz-Montero ME, Cabestrero Ó, Rodríguez-Aranda J. 2013. Hydromagnesite precipitation in microbial mats from a highly alkaline lake. Cent Spain Mineral Mag 77:26–28.

Sanz-Montero ME, Cabestrero O, Sánchez-Román M. 2019. Microbial Mg-rich carbonates in an extreme alkaline lake (Las Eras, Central Spain). Front Microbiol 10:148.

Sanz-Montero ME, Rodríguez-Aranda JP. 2012. Magnesite formation by microbial activity: evidence from a Miocene hypersaline lake. Sediment Geol 263:6–15.

Schloss PD, Gevers D, Westcott SL. 2011. Reducing the effects of PCR amplification and sequencing artifacts on 16S rRNA-based studies. PLoS One 6(12):e27310.

Schopf JW. 2006. Fossil evidence of Archaean life. Phil Trans R Soc B B361:869–885.

Schopf JW, Walter M, Ruiji R. 2007. Earliest evidence of life on Earth. Precambrian Res 158(3–4):139–140.

Schopf JW, Packer BM. 1987. Early Archean (3.3-billion to 3.5-billion-year-old) microfossils from Warrawoona Group, Australia. Science 237(4810):70–73.

Schouten S, Hopmans EC, Sinninghe Damsté JS. 2013. The organic geochemistry of glycerol dialkyl glycerol tetraether lipids: a review. Org Geochem 54:19–61.

Schouten S, van der Meer MTJ, Hopmans EC, Rijpstra WIC, Reysenbach AL, Ward DM, Sinninghe Damsté JS. 2007. Archaeal and bacterial glycerol dialkyl glycerol tetraether lipids in hot springs of Yellowstone National Park. Appl Env Microbiol 73(19):6181–6191.

Scherf AK, Rullkötter J. 2009. Biogeochemistry of high salinity microbial mats – Part 1: lipid composition of microbial mats across intertidal flats of Abu Dhabi, United Arab Emirates. Org Geochem 40:1018–1028.

Shiraishi F, Bissett A, D. de Beer, Reimer A, Arp G. 2008. Photosynthesis, respiration and exopolymer calcium-binding in biofilm calcification (Westerhöfer and Deinschwanger Creek, Germany). Geomicrobiol J 25:83–94.

Shirokova LS, Mavromatis V, Bundeleva IA, Pokrovsky OS, Bénézeth P, Gérard E, Pearce CR, Oelkers EH. 2013. Using Mg isotopes to trace cyanobacterially mediated magnesium carbonate precipitation in alkaline lakes. Aquat Geochem 19(1):1–24.

Shirokova LS, Mavromatis V, Bundeleva IA, Pokrovsky OS, Bénézeth P, Pearce C, Gerard E, Balor S, Oelkers EH. 2011. Can Mg isotopes be used to trace cyanobacteria-mediated magnesium carbonate precipitation in alkaline lakes? Biogeosci Disc 8(4):6473–6517.

Sinninghe Damsté JS, Rijpstra WIC, Hopmans EC, Weijers JWH, Foesel BU, Overmann J, Dedysh SN. 2011. 13,16-Dimethyl octacosanedioic acid (iso-diabolic acid), a common membrane-spanning lipid of acidobacteria subdivisions 1 and 3. Appl Environ Microbiol 77(12):4147–4154.

Souza V, Siefert JL, Escalante AE, Elser JJ, Eguiarte LE. 2012. The cuatro ciénegas basin in Coahuila, Mexico: an astrobiological precambrian park. Astrobiology 12(7):641–647.

Summons RE, Jahnke LL, Roksandic Z. 1994. Carbon isotopic fractionation in lipids from methanotrophic bacteria: relevance for interpretation of the geochemical record of biomarkers. Geochim Cosmochim Acta 58:2853–2863.

Sun Y, Cai Y, Huse SM, Knight R, Farmerie WG, Wang X, Mai V. 2012. A large-scale benchmark study of existing algorithms for taxonomy- independent microbial community analysis. Brief Bioinformatics 13(1):107–121.

Thiel V, Merz-Preiß M, Reitner J, Michaelis W. 1997. Biomarker studies on microbial carbonates: extractable lipids of a calcifying cyanobacterial mat (Everglades, USA). Facies 36(1):163–172.

Visscher PT, Reid RP, Bebout BM, Hoeft SE, Macintyre IG, Thompson JA. 1998. Formation of lithified micritic laminae in modern marine stromatolites (Bahamas): the role of sulfur cycling. Am Mineral 83(11–12):1482–1493.

Visscher PT, Stolz JF. 2005. Microbial mats as bioreactors: populations, processes, and products. Palaeogeogr Palaeoclimatol Palaeoecol 219(1–2):87–100.

Volkman JK. 1986. Biological marker compounds as indicators of the depositional environments of petroleum source rocks. In: Fleet, AJ, Kelts, K, Talbot, MR, editors. Petroleum Source Rocks. London, UK: Geological Society London Special Publication, p103–122.

Volkman JK, Barrett SM, Blackburn SI, Mansour MP, Sikes EL, Gelin F. 1998. Microalgal biomarkers: a review of recent research developments. Org Geochem 29(5–7):1163–1179.

Volkman JK, Maxwell JR. 1986. Acyclic isoprenoids as biological markers. In: Johns, RB, editor. Biological Markers in the Sedimentary Record. Oxford, UK: Elsevier, p1–42.

Wacey D, Kilburn MR, Saunders M, Cliff J, Brasier MD. 2011. Microfossils of sulfur metabolizing cells in ∼3.4 billion year old rocks of Western Australia. Nature Geosci 4(10):698–670.

Weijers JWH, Schouten S, Hopmans EC, Geenevasen JAJ, David ORP, Coleman JM, Pancost RD, Sinninghe Damsté JS. 2006. Membrane lipids of mesophilic anaerobic bacteria thriving in peats have typical archaeal traits. Environ Microbiol 8(4):648–657.

Yang B, Xu-Jing G, Yun-Zhen L, Tao H. 2017. Experimental and visual research on the microbial induced carbonate precipitation by *Pseudomonas aeruginosa*. AMB Express 7:57.

Zeyen N, Benzerara K, Li J, Groleau A, Balan E, Robert JL, Esteve I, Tavera R, Moreira D. Lopez-Garcıa P. 2015. Formation of low-T hydrated silicates in modern microbialites from Mexico and implications for microbial fossilization. Frontiers Earth Sci 3.

Zhang CL, Wang J, Dodsworth J, Williams AJ, Zhu C, Hinrichs KU, Zheng F, Hedlund BP. 2013. In situ production of branched glycerol dialkyl glycerol tetraethers in a great basin hot spring (USA). Front Microbiol 4:181.